Title: ESCRT recruitment to mRNA-encoded SARS-CoV-2 spike induces virus-like particles and enhanced antibody responses

Authors: Magnus A. G. Hoffmann[1*], Zhi Yang[1‡], Kathryn E. Huey-Tubman[1], Alexander A. Cohen[1], Priyanthi N. P. Gnanapragasam[1], Leesa M. Nakatomi[1], Kaya N. Storm[1], Woohyun J. Moon[2], Paulo J.C. Lin[2], Pamela J. Bjorkman[1*]

Affiliations:

[1]Division of Biology and Biological Engineering, California Institute of Technology, Pasadena, CA 91125, USA

[2]Acuitas Therapeutics, Vancouver, BC, V6T 1Z3, CANADA

‡Present address: Department of Molecular and Cell Biology, University of California, Berkeley, CA 94720, USA

*To whom correspondence should be addressed: Email: mhoffman@caltech.edu, bjorkman@caltech.edu

Summary

Prime-boost regimens for COVID-19 vaccines elicit poor antibody responses against Omicron-based variants and employ frequent boosters to maintain antibody levels. We present a natural infection-mimicking technology that combines features of mRNA- and protein nanoparticle-based vaccines through encoding self-assembling enveloped virus-like particles (eVLPs). eVLP assembly is achieved by inserting an ESCRT- and ALIX-binding region (EABR) into the SARS-CoV-2 spike cytoplasmic tail, which recruits ESCRT proteins to induce eVLP budding from cells. Purified spike-EABR eVLPs presented densely-arrayed spikes and elicited potent antibody responses in mice. Two immunizations with mRNA-LNP encoding spike-EABR elicited potent CD8+ T-cell responses and superior neutralizing antibody responses against original and variant SARS-CoV-2 compared to conventional spike-encoding mRNA-LNP and purified spike-EABR eVLPs, improving neutralizing titers >10-fold against Omicron-based variants for three months post-boost. Thus, EABR technology enhances potency and breadth of vaccine-induced responses through antigen presentation on cell surfaces and eVLPs, enabling longer-lasting protection against SARS-CoV-2 and other viruses.

Introduction

mRNA vaccines emerged during the COVID-19 pandemic as an ideal platform for the rapid development of effective vaccines (Corbett et al., 2020). Currently approved SARS-CoV-2 mRNA vaccines encode the viral spike (S) trimer (Zheng et al., 2022), the primary target of neutralizing antibodies during natural infections (Chen et al., 2022). Clinical studies have demonstrated that mRNA vaccines are highly effective, preventing >90% of symptomatic and severe SARS-CoV-2 infections (Baden et al., 2021; Polack et al., 2020) through both B and T cell responses (Kent et al., 2022). mRNA vaccines in part mimic an infected cell since expression of S within cells that take up S-encoding mRNAs formulated in lipid nanoparticles (LNP) (Hogan and Pardi, 2022) results in cell surface expression of S protein to stimulate B cell activation. Translation of S protein inside the cell also provides viral peptides for presentation on MHC class I molecules to cytotoxic T cells, which does not commonly occur in protein nanoparticle-based vaccines (Rock et al., 2016) that resemble the virus by presenting dense arrays of S protein; e.g., the Novavax NVX-CoV2373 vaccine (Heath et al., 2021; Keech et al., 2020). However, comparisons to COVID-19 mRNA vaccines showed that NVX-CoV2373 elicits comparable neutralizing antibody titers (Karbiener et al., 2022; Zhang et al., 2022), the main immune correlate of vaccine-induced protection (Barouch, 2022), suggesting that potent B cell activation can be achieved through presentation of viral surface antigens on cell surfaces or virus-resembling nanoparticles. Achieving higher antibody neutralization titers is desirable as antibody levels contract substantially over a period of several months (Zhang et al., 2022), and SARS-CoV-2 variants of concern (VOCs) that are less sensitive to antibodies elicited by vaccines or natural infection have been emerging (Chen et al., 2021; Hachmann et al., 2022; Wu et al., 2021). An optimal vaccine might therefore combine attributes of

both mRNA- and protein nanoparticle-based vaccines by delivering a genetically encoded S protein that gets presented on cell surfaces and induces self-assembly and release of S-presenting nanoparticles.

Here, we describe a novel technology that engineers membrane proteins to induce self-assembly of enveloped virus-like particles (eVLPs) that bud from the cell surface. This is accomplished for the SARS-CoV-2 S protein by inserting a short amino acid sequence (termed an ESCRT- and ALIX-binding region or EABR) (Lee et al., 2008) at the C-terminus of its cytoplasmic tail to recruit host proteins from the endosomal sorting complex required for transport (ESCRT) pathway. Many enveloped viruses recruit ESCRT-associated proteins such as TSG101 and/or ALIX through capsid or other interior viral structural proteins during the budding process (McCullough et al., 2018; Votteler and Sundquist, 2013). Thus, fusing the EABR to the cytoplasmic tail of a viral glycoprotein or other membrane protein directly recruits TSG101 and ALIX, bypassing the need for co-expression of other viral proteins for eVLP self-assembly. Cryo-electron tomography (cryo-ET) showed dense coating of spikes on purified S-EABR eVLPs, and direct injections of the eVLPs elicited potent neutralizing antibody responses in mice. Finally, we demonstrate that an mRNA vaccine encoding the S-EABR construct elicited at least 5-fold higher neutralizing antibody responses against SARS-CoV-2 and VOCs in mice than a conventional S-encoding mRNA vaccine or purified S-EABR eVLPs. These results demonstrate that mRNA-mediated delivery of S-EABR eVLPs elicits superior antibody responses, suggesting that dual presentation of viral surface antigens on cell surfaces and on extracellular eVLPs has the potential to enhance the effectiveness of COVID-19 mRNA vaccines.

Results

ESCRT recruitment to the spike cytoplasmic tail induces eVLP assembly

To evaluate the hypothesis that direct recruitment of ESCRT proteins to the cytoplasmic tail of a SARS-CoV-2 S protein could result in self-assembly and budding of eVLPs, we fused EABRs derived from different sources to the truncated cytoplasmic tail of the S protein, separated from its C-terminus by a short Gly-Ser linker (Figures 1A and 1B). The S protein contained the D614G substitution (Korber et al., 2020), a furin cleavage site, two proline substitutions (2P) in the S2 subunit to stabilize the prefusion conformation (Pallesen et al., 2017), and the C-terminal 21 residues were truncated to optimize cell surface expression by removing an endoplasmic reticulum (ER)-retention signal (ΔCT) (McBride et al., 2007) (Figure 1B). We evaluated the EABR fragment from the human CEP55 protein that binds TSG101 and ALIX during cytokinesis (Lee et al., 2008) (Figure 1B). For comparisons, viral late domains that recruit early ESCRT proteins during the viral budding process were obtained from the Equine Infectious Anemia Virus (EIAV) p9 protein (Fisher et al., 2007), residues 1-44 of the Ebola virus (EBOV) VP40 protein (Madara et al., 2015), and the HIV-1 p6 protein (Fujii et al., 2009) (Figure S1A). We hypothesized that eVLP production could be enhanced by preventing endocytosis of EABR-fusion proteins to extend the duration that proteins remain at the plasma membrane to interact with ESCRT proteins. We therefore added an endocytosis prevention motif (EPM), a 47-residue insertion derived from the murine Fc gamma receptor FcgRBII-B1 cytoplasmic tail (Figures 1A and 1B) that tethers FcgRBII-B1 to the cytoskeleton to prevent coated pit localization and endocytosis (Miettinen et al., 1989).

The abilities of the S-EABR, S-p9, S-VP40$_{1-44}$, and S-p6 constructs to generate eVLPs were evaluated by transfecting Expi293F cells and measuring eVLP production in supernatants from which eVLPs were purified by ultracentrifugation on a 20% sucrose cushion. Western blot analysis showed that the highest S protein levels were detected for the S-EABR construct, suggesting that the CEP55 EABR induced efficient self-assembly of S-containing eVLPs (Figures 1C and S1B). At a sample dilution of 1:400, the S-EABR construct produced a similarly intense band compared to the S-p9 construct at a 1:40 dilution, suggesting that S protein levels were ~10-fold higher. The CEP55 EABR binds both ALIX and TSG101 (Lee et al., 2008), whereas EIAV p9 only binds ALIX (Fisher et al., 2007), suggesting that optimal recruitment of both ESCRT proteins is required for efficient eVLP assembly. The S-p6 and S-VP40$_{1-44}$ samples contained little or no S protein suggesting that eVLP assembly was inefficient, possibly resulting from lower affinities for ESCRT proteins (Figures 1C and S1B).

We further characterized the S-EABR construct by experimenting with different EABR sequences (Figure S1A), finding that addition of a second EABR domain (S-2xEABR) reduced eVLP production (Figure 1D). To investigate whether S-EABR eVLP assembly is dependent on ESCRT recruitment, we generated S-EABR$_{mut}$ by substituting an EABR residue (Tyr187 in CEP55) that is essential for interacting with ALIX (Lee et al., 2008) (Figure S1A). While the purified S-EABR eVLP sample produced an intense band at a 1:200 dilution, no band was detected for S-EABR$_{mut}$ at a 1:20 dilution, suggesting that eVLP production was abrogated for S-EABR$_{mut}$ and highlighting the importance of ALIX recruitment for eVLP assembly (Figure 1D). To identify the minimal EABR sequence required for eVLP assembly, we designed S constructs fused to the complete EABR domain (CEP55$_{170-213}$), EABR$_{min1}$ (CEP55$_{180-}$

$_{213}$), and $EABR_{min2}$ ($CEP55_{180-204}$) (Figure S1a). While S-EABR eVLP yields were diminished for $EABR_{min2}$, production efficiency was retained for $EABR_{min1}$ (Figure 1E). To assess the effects of the EPM within the cytoplasmic tail of the S-EABR construct, we evaluated eVLP production for an S-EABR construct that did not include the EPM. Western blot analysis demonstrated that increased amounts of S protein were detected after eVLP purification from cells transfected with S-EABR compared to S-EABR/no EPM, suggesting that the EPM enhances eVLP production (Figure 1F).

We also compared the S-EABR construct to other eVLP approaches (Martins et al., 2022) that require co-expression of S protein with structural viral proteins, such as HIV-1 Gag (Hoffmann et al., 2020) or the SARS-CoV-2 M, N, and E proteins (Syed et al., 2021). Western blot analysis showed that purified S-EABR eVLP fractions contained at least 10-fold more S protein than eVLPs produced by co-expression of S and Gag or S, M, N, and E (Figure 1G), suggesting that S-EABR eVLPs assemble and/or incorporate S proteins more efficiently than the other eVLP approaches. Purified S-EABR eVLPs also contained higher levels of S protein compared to S-ferritin nanoparticles purified from transfected cell supernatants, which have been shown to elicit potent immune responses in animal models (Joyce et al., 2021; Powell et al., 2021) (Figure 1G).

3D reconstructions derived from cryo-ET showed purified S-EABR eVLPs with diameters ranging from 40 - 60 nm that are surrounded by a lipid bilayer and the majority of which were densely coated with spikes (Figures 1H and 1I; Movie S1). To estimate the number of S trimers, we counted trimer densities in ~4 nm computational tomographic slices of individual eVLPs, finding ~10-40 spikes per particle that were

heterogeneously distributed on the surface of eVLPs. The upper limit of the number of spikes on eVLPs roughly corresponds to spike numbers on larger SARS-CoV-2 virions (>100 nm in diameter) (Ke et al., 2020); thus, the spike densities on the majority of eVLPs exceed those on authentic viruses. Spikes on eVLPs were separated by distances of ~20-26 nm (measured between the centers of trimer apexes) for densely coated particles (Figures 1H and 1I). To assess the general applicability of the EABR approach, we also generated EABR eVLPs for HIV-1 Env, which produced eVLPs with higher Env content than co-expression of Env and HIV-1 Gag (Figure S1C), and for the multi-pass transmembrane protein CCR5 (Figure S1D). Taken together, these results are consistent with efficient incorporation of S proteins into S-EABR eVLPs that are released from transfected cells and suggest that the EABR technology can be applied to a wide range of membrane proteins.

S-EABR eVLPs induce potent antibody responses in immunized mice

The potential of purified S-EABR eVLPs as a vaccine candidate against SARS-CoV-2 was evaluated in C57BL/6 mice (Figure 2A). S-EABR eVLPs were purified from transfected cell supernatants by ultracentrifugation on a 20% sucrose cushion followed by size exclusion chromatography (SEC), and S protein concentrations were determined by quantitative Western blot analysis (Figures S2A and S2B). For a 100 mL transfection of Expi293F cells, purified S-EABR eVLPs from supernatants contained ~250-500 µg S protein. Immunizations with S-EABR eVLPs were compared to purified soluble S and to soluble S covalently attached to SpyCatcher-mi3 protein nanoparticles (S-mi3) (Keeble et al., 2019). 0.1 µg doses (calculated based on S protein content) were administered by subcutaneous injections on days 0 and 28 for all immunogens in the presence of Sigma adjuvant (Figure 2A), and we evaluated

serum antibody responses by enzyme-linked immunosorbent assays (ELISAs) and in vitro pseudovirus neutralization assays. After the prime, S-EABR eVLPs elicited robust antibody binding and neutralization responses in all mice against SARS-CoV-2 (WA1 variant including the D614G substitution (WA1/D614G)), similar to titers elicited by S-mi3 (Figures 2B and 2C). In contrast, no neutralizing antibody responses were detected for soluble S protein immunization after the prime. Neutralizing antibody titers elicited by S-EABR eVLPs and S-mi3 increased by >10-fold after boosting and were >20-fold higher than titers measured for soluble S (Figure 2C). S-EABR eVLPs elicited potent antibody responses targeting the receptor-binding domain (RBD) of the S protein (Figure S2C), a primary target of anti-SARS-CoV-2 neutralizing antibodies (Kleanthous et al., 2021). Serum responses were also evaluated against authentic SARS-CoV-2 by plaque reduction neutralization tests (PRNTs), showing robust neutralizing activity against SARS-CoV-2 WA1 (Figure S2D). Neutralization titers dropped ~4-fold and ~2-fold against the SARS-CoV-2 Beta and Delta variants, respectively, consistent with studies of licensed vaccines that encode the SARS-CoV-2 WA1 S protein (van Gils et al., 2022). These results demonstrate that purified S-EABR eVLPs elicit potent immune responses in vivo and represent an alternative technology for producing nanoparticle-based vaccines that does not involve detergent-mediated cell lysis and separation of membrane protein antigens from cell lysates, as required for protein nanoparticle vaccines such as NVX-CoV2373, a COVID-19 vaccine (Heath et al., 2021; Keech et al., 2020), or FluBlok, an influenza vaccine (Cox and Hollister, 2009).

mRNA-encoded S-EABR construct induces cell surface expression and eVLP budding

A key advantage of the EABR eVLP technology over existing nanoparticle-based vaccine approaches is that S-EABR constructs can be easily delivered as mRNA vaccines since both eVLP assembly and cell surface expression only require expression of a single genetically encoded component. While conventional COVID-19 mRNA vaccines induce antibody responses through cell surface expression of S protein (Figure 3A, top), mRNA-mediated delivery of an S-EABR construct could enhance B cell activation because S-EABR proteins will not only be expressed at the cell surface – they will also induce assembly of eVLPs that bud from the cell and distribute inside the body to activate immune cells (Figure 3A, bottom).

To investigate whether genetic encoding of S-EABR eVLPs enhances the potency of a SARS-CoV-2 S-based mRNA vaccine, we started by synthesizing nucleoside-modified mRNAs encoding S, S-EABR, S-EPM, or S-EABR/no EPM. Cell surface expression and eVLP assembly were evaluated by flow cytometry and Western blot analysis 48 hours after in vitro transfection of mRNAs in HEK293T cells, demonstrating higher surface expression for S compared to the S-EABR fusion protein (Figure 3B). While addition of the EPM had little effect on S surface expression, removal of the EPM lowered surface levels for the S-EABR construct. Western blot analysis of supernatants confirmed that the S and S-EPM transfections did not generate detectable eVLPs in supernatants, whereas eVLPs were strongly detected in supernatants from S-EABR transfected cells (Figure 3C). eVLP production was decreased for S-EABR/no EPM, which together with the flow cytometry results (Figure

3B), suggests that EPM addition enhances both S-EABR cell surface expression and eVLP assembly.

The observed reduction in S cell surface expression in the S-EABR versus S mRNA transfections could be caused by lower overall cell surface expression of the S-EABR fusion protein, incorporation of S-EABR proteins into eVLPs that bud from the cell surface, or both. To evaluate these possibilities, we calculated approximate numbers of S trimers expressed from the S-EABR construct. Assuming that $3x10^6$ cells were transfected (6-well plate) and up to $1x10^5$ S trimers were expressed on the surface of each cell (based on the approximate number of B cell receptors on a B cell (Alberts et al., 2002)), transfected cell surfaces would contain ~0.5 pmol or ~70 ng of total S protein. Supernatant samples for Western blots were concentrated to a final volume of 200 µL of which 1.2 µL was loaded onto a gel. As the detection limit for S1 is ~20 ng, the Western blot analysis suggested that purified S-EABR eVLPs from transfected cell supernatants contained at least ~17 ng/µL S protein, corresponding to >3 µg S protein in the purified transfected cell supernatant. These calculations suggested that the observed reduction in cell surface expression for the S-EABR construct was at least partially caused by incorporation of S-EABR proteins into budding eVLPs that were released into the supernatant. Given that the estimated S protein content on released eVLPs exceeded the approximate amount of S protein presented on cell surfaces, it is possible that the S-EABR construct induces higher overall expression of S antigens compared to S for which expression is restricted to cell surfaces. Taken together, the mRNA transfection results demonstrate that the mRNA-encoded S-EABR construct enables dual presentation of S antigens on cell surfaces and released eVLPs.

S-EABR mRNA-LNP elicit superior antibody titers compared to conventional vaccines

The effect of eVLP production on mRNA vaccine potency was evaluated in BALB/c mice by comparing mRNAs encoding S or S-EABR constructs that were encapsulated in LNP (Figure 4A). As described for preclinical studies of a COVID-19 mRNA vaccine in mice (Corbett et al., 2020), mRNA-LNP were administered intramuscularly (IM) at a dose of 2 µg mRNA on days 0 and 28. mRNA-LNP immunizations were also compared to purified S-EABR eVLPs that were injected IM in the presence of Addavax adjuvant. Antibody binding and neutralizing responses were evaluated by ELISAs and pseudovirus neutralization assays, respectively (Figures 4B-4H). After the prime, S and S-EABR mRNA-LNP elicited significantly higher antibody binding responses against the SARS-CoV-2 S protein than purified S-EABR eVLPs (Figure 4C). However, the highest neutralizing antibody titers were elicited by purified S-EABR eVLPs, which were significantly higher than titers elicited by the S mRNA-LNP (Figure 4D).

After a boost immunization, S-EABR mRNA-LNP elicited significantly higher binding and neutralizing antibody titers than purified S-EABR eVLPs and S mRNA-LNP (Figures 4B-4D). Geometric mean neutralization titers measured for S-EABR mRNA-LNP were 5.1- and 5-fold higher than titers elicited by purified S-EABR eVLPs and S mRNA-LNP, respectively (Figures 4B and 4D). Three months post-boost (day 112), mean neutralization titers were 5.9- and 6.8-fold higher for S-EABR mRNA-LNP compared to purified S-EABR eVLPs and S mRNA-LNP, respectively, demonstrating that the increased serum neutralization activity was maintained (Figures 4B and 4D).

We also evaluated serum neutralizing activity against SARS-CoV-2 VOCs. S-EABR mRNA-LNP elicited 4.9- and 6.5-fold higher mean neutralizing responses against the Delta variant compared to S mRNA-LNP, as well as 4.6- and 9.4-fold higher titers compared to purified S-EABR eVLPs on days 56 and 112, respectively (Figures 4B and 4E). Against Omicron BA.1, neutralizing antibody responses dropped markedly for all groups, except for mice that received S-EABR mRNA-LNP, which elicited 15.1- and 9.5-fold higher neutralizing titers than S mRNA-LNP and 20.7- and 15.4-fold higher titers than purified S-EABR eVLPs on days 56 and 112, respectively (Figures 4B and 4F). Against Omicron BA.2, mean neutralization titers measured for mice that received S-EABR mRNA-LNP were also 10.9- and 8.2-fold higher compared to S mRNA-LNP and 7- and 12.2-fold higher compared to purified S-EABR eVLPs on days 56 and 112, respectively (Figures 4B and 4G). Compared to BA.2 titers, neutralizing antibody responses against the BA.4/5 variant decreased 4-8-fold for mice that received S-EABR mRNA-LNP, but titers were still 3.4- and 4-fold higher (but not statistically significant) compared to S mRNA-LNP and 4.2- and 6.8-fold higher compared to purified S-EABR eVLPs on days 56 and 112, respectively (Figures 4B and 4H). While neutralization titers of >1:400 against the BA.4/5 variant were measured for 7 of 10 mice that received S-EABR mRNA-LNP on day 56, such responses were only detected in 1 or 2 mice that received purified S-EABR eVLPs or S mRNA-LNP, respectively. Together, these results demonstrate that mRNA-mediated delivery of S-EABR eVLPs enhances the potency and breadth of humoral immune responses in mice compared to conventional mRNA and protein nanoparticle-based vaccine approaches. The observed improvements in neutralizing activity against Omicron-based VOCs were substantially larger than the 1.5-fold increases reported for recently approved bivalent mRNA booster shots (Khoury et al., 2022),

suggesting that S-EABR mRNA-LNP-based booster immunizations could induce more effective and lasting immunity against Omicron-based and emerging VOCs than current COVID-19 vaccines.

S-EABR mRNA-LNP induce potent T cell responses

On day 112 (3 months post-boost), splenocytes were isolated from immunized mice to analyze T cell responses by enzyme-linked immunosorbent spot (ELISpot) assays (Ranieri et al., 2014). Splenocytes were stimulated with a pool of SARS-CoV-2 S-specific peptides, and INF-γ and IL-4 secretion were measured to evaluate T cell activation. mRNA-LNP encoding S and S-EABR constructs induced potent INF-γ responses, consistent with the presence of S-specific cytotoxic CD8+ T cells and T helper 1 (T_H1) cellular immune responses (Figure 5A). In contrast, INF-γ responses were almost undetectable for mice immunized with purified S-EABR eVLPs (Figure 5A). These results were expected as mRNA-LNP immunizations result in intracellular expression of S or S-EABR immunogens and MHC class I presentation of antigenic peptides that activate CD8+ T cells, which does not commonly occur for protein nanoparticle-based vaccines (Rock et al., 2016).

S-EABR mRNA-LNP induced significantly stronger IL-4 responses compared to S mRNA-LNP and purified S-EABR eVLPs (Figure 5B), consistent with potent T_H2 cellular immune responses. While T_H1- and T_H2-biased responses were observed for S mRNA-LNP and purified S-EABR eVLPs, respectively, S-EABR mRNA-LNP induced a balanced T_H1/T_H2 response, thereby potently stimulating cellular and humoral immune responses. Thus, S-EABR mRNA-LNP retain the ability of conventional S mRNA-LNP to activate potent cytotoxic CD8+ T cell responses, while

also potently activating T_H2 CD4+ T cell responses to enhance humoral immune responses leading to increased antibody potency and breadth.

Discussion

Here, we present a novel technology to generate eVLPs for vaccine and other applications. The approach harnesses the ESCRT pathway that is involved in cell division and viral budding (McCullough et al., 2018; Votteler and Sundquist, 2013) to drive assembly and release of eVLPs that present membrane proteins containing a cytoplasmic ESCRT-recruiting motif, the EABR sequence from the human centrosomal protein CEP55 (van der Horst et al., 2009). Our results demonstrate that the EABR-based platform produces eVLPs that incorporate higher levels of membrane antigens compared to approaches that require co-expression of the antigen with viral capsid proteins such as Gag or with the SARS-CoV-2 M, N, and E proteins. Purified S-EABR eVLPs elicited potent antibody responses against SARS-CoV-2 in mice that were similar in magnitude to those elicited by a 60-mer protein nanoparticle displaying S trimers. Compared to existing protein nanoparticle-based vaccine approaches, the EABR technology exhibits attractive manufacturing properties as (*i*) eVLP production requires expression of only a single component, (*ii*) transmembrane proteins are retained in their native membrane-associated conformation to ensure optimal protein expression and stability, and (*iii*) fully assembled eVLPs can be purified directly from culture supernatants without requiring detergent-mediated cell lysis and separation of membrane protein antigens from cell lysates. The lipid bilayer surrounding eVLPs also prevents off-target antibody responses against a nanoparticle scaffold that have been reported for protein nanoparticle-based immunogens (Kraft et al., 2022). Due to its modularity, flexibility, and versatility, the EABR technology could potentially be used

to generate eVLPs presenting a wide range of surface proteins for vaccine and therapeutic applications.

To optimize the EABR technology, we evaluated several ESCRT-recruiting motifs for their ability to drive eVLP assembly, including viral late domains from EIAV, HIV-1, and EBOV. The EABR from CEP55 generated eVLPs 10-fold more efficiently than the EIAV late domain p9. The EABR binds to ESCRT proteins ALIX and TSG101 (Lee et al., 2008), while p9 binds only to ALIX (Fisher et al., 2007), suggesting that efficient eVLP assembly requires recruitment of both proteins. HIV-1 p6 contains motifs that interact with both TSG101 and ALIX (Fisher et al., 2007; Fujii et al., 2009), but S-p6 constructs did not induce detectable eVLP budding in our experiments, perhaps because reported affinities are relatively low (Fisher et al., 2007; Pornillos et al., 2002) compared to TSG101 and ALIX affinities reported for the EABR (Lee et al., 2008). eVLP production might be optimized by designing ESCRT-binding motifs with increased affinities for ESCRT proteins. We were able to enhance eVLP production by including an EPM derived from the FcgRII-B1 cytoplasmic tail (Miettinen et al., 1992) to reduce endocytosis of EABR-fusion proteins, which increased S-EABR cell surface expression and eVLP production.

An advantage of the EABR technology is that constructs can be easily delivered as mRNA vaccines since eVLP assembly requires expression of only a single component. This strategy results in presentation of viral surface antigens on the cell surface and on released eVLPs that could distribute throughout the body, thereby combining immune responses elicited by both conventional mRNA and protein nanoparticle-based vaccines. S-EABR mRNA-LNP elicited significantly higher binding

385 and neutralizing antibody responses compared to conventional S-based mRNA-LNP
386 analogous to current COVID-19 mRNA vaccines and to purified S-EABR eVLPs,
387 suggesting that dual presentation of viral surface antigens on cell surfaces and eVLPs
388 potentiates B cell activation. Presentation of viral surface antigens on cell surfaces
389 alone potentially restricts expression for conventional mRNA vaccines due to a finite,
390 and presumably limited, environment for insertion of both delivered and endogenous
391 membrane proteins. Thus, combining cell surface expression and eVLP release for
392 the S-EABR mRNA-LNP may increase overall presentation of viral surface antigens
393 to the immune system. It is also possible that mRNA-mediated S-EABR eVLP
394 production expands the biodistribution of viral surface antigens to more effectively
395 engage B cells in lymph nodes distant from the injection site. The enhanced humoral
396 immune responses elicited by S-EABR mRNA-LNP were consistent with potent T_H2
397 cellular responses observed in S-EABR mRNA-LNP-immunized mice, which were
398 more pronounced than in mice immunized with S mRNA-LNP or purified S-EABR
399 eVLPs. Importantly, cytotoxic CD8+ T cell responses were maintained in S-EABR
400 mRNA-LNP- compared to S mRNA-LNP-immunized animals. Thus, S-EABR mRNA-
401 LNP potently stimulate both cellular and humoral immune responses.
402
403 The higher peak antibody levels elicited by the S-EABR mRNA-LNP would likely
404 impact the durability of protective antibody responses. Notably, differences in serum
405 antibody titers across different immunizations were maintained until three months
406 post-boost, suggesting that antibody levels might contract at similar rates for the tested
407 vaccine types. Hence, the elevated peak antibody titers elicited by the S-EABR mRNA-
408 LNP could result in markedly prolonged periods of immune protection compared to
409 conventional vaccine approaches, which could minimize the need for frequent booster

410 immunizations. Long-term studies that monitor antibody levels for several months are
411 needed to elucidate the relationship between peak antibody titers and durability of
412 responses.
413
414 Two immunizations with S-EABR mRNA-LNP also elicited potent neutralizing antibody
415 responses against SARS-CoV-2 Delta and Omicron-based VOCs, suggesting that
416 higher antibody responses could lead to enhanced protection against viral escape
417 variants. The conventional S-based mRNA-LNP immunization only elicited weak
418 responses against Omicron-based VOCs, consistent with outcomes reported in
419 humans in which weak Omicron-specific responses to WA1-based vaccines were
420 enhanced after a 3rd immunization (Barouch, 2022; Gruell et al., 2022). S-EABR
421 mRNA-LNP elicited >10-fold higher neutralizing antibody titers against Omicron BA.1
422 and BA.2 VOCs compared to S mRNA-LNP after only two immunizations, suggesting
423 that the simple addition of a short EABR-encoding sequence to the spike gene in
424 current mRNA vaccines could have limited the global spread of Omicron-based VOCs.
425 Our results also suggest that S-EABR mRNA-LNP-based booster immunizations
426 would induce superior immunity against Omicron-based and emerging VOCs
427 compared with current boosting strategies, as bivalent booster shots that contain
428 ancestral and Omicron-based variants improve neutralizing antibody titers by only 1.5-
429 fold compared to conventional booster shots (Khoury et al., 2022). Future studies need
430 to investigate whether the observed increase in neutralization activity against
431 Omicron-based VOCs results from higher overall antibody levels and/or increased
432 antibody targeting of sub-immunodominant conserved epitopes on S trimer.
433

Enhanced antibody responses compared to S mRNA-LNP have also been reported for co-delivery of mRNAs encoding SARS-CoV-2 S, M, and E proteins, which should result in dual presentation of S on cell surfaces and released eVLPs (Lu et al., 2020). However, higher mRNA doses (10 µg) were needed to deliver all three mRNAs, and only modest improvements (~2.5-fold) in neutralizing antibody titers were achieved. Our results showed that S-EABR eVLPs assemble more efficiently in vitro than eVLPs driven by co-expression of S, M, N, and E proteins, potentially explaining why S-EABR mRNA-LNP induced larger increases in antibody titers at lower doses. Co-delivery of multiple mRNAs also poses an obstacle for vaccine manufacturing, whereas COVID-19 and other mRNA vaccines could be easily modified to generate eVLPs by adding a short sequence containing EABR and EPM motifs to the cytoplasmic domains of the encoded immunogens. mRNA delivery of a trimerized RBD-ferritin fusion construct, which should result in secretion of non-enveloped ferritin nanoparticles displaying trimeric RBDs without cell surface expression of RBDs, has also been reported (Sun et al., 2021). This approach was not compared to a conventional S mRNA-LNP-based immunogen, highlighting the need for comparison studies of different vaccine approaches to elucidate the individual effects of antigen presentation on cell surfaces and virus-like nanoparticles on the magnitude and quality of immune responses.

In summary, we present a novel technology to efficiently generate eVLPs for vaccine and other therapeutic applications. We demonstrate that an mRNA vaccine encoding SARS-CoV-2 spike-EABR eVLPs elicits antibody responses with enhanced potency and breadth compared to conventional vaccine strategies in mice, which warrants further investigation in other preclinical animal models and humans as a vaccine strategy.

Acknowledgements

We thank J. Vielmetter and the Caltech Protein Expression Center for assistance with protein production, K. Dam for biotinylated proteins for ELISAs, M. Anaya for a BirA expression plasmid, and J. Bloom (Fred Hutchinson) and P. Bieniasz (Rockefeller University) for neutralization assay reagents. We thank J. Keeffe, A. West, Y. Tam (Acuitas Therapeutics), C. Barnes (Stanford), H. Kleanthous (Bill and Melinda Gates Foundation), B. Wold, G. Tolomiczenko, and the Caltech Merkin Institute for Translational Research for helpful discussions and A. West for careful reading of the manuscript. Electron tomography was performed in the Caltech Cryo-EM Center with assistance from S. Chen. We thank Labcorp Drug Development–Antibody Reagents and Vaccines (Denver, PA) (formerly Covance, Inc.) for mouse immunization studies, BIOQUAL, Inc. (Rockville, MD) for PRNT50 assays, and R. Sukhovershin and RNAcore (Houston Methodist Research Institute) for synthesis of mRNAs and helpful discussion. Figures 1A and 3A were created with Biorender.com. This work was supported by the Bill and Melinda Gates Foundation INV-034638 (P.J.B.), the Caltech Merkin Institute (P.J.B.), the George Mason University Fast Grants (P.J.B.), the Rothenberg Innovation Initiative (RI^2) (P.J.B.), and Wellcome Leap (P.J.B.). M.A.G.H. was supported by an NIH Director's Early Independence Award (FAIN# DP5OD033362).

Author contributions:

M.A.G.H. and P.J.B. conceived the study, acquired funding, analyzed the data, and wrote the manuscript with contributions from other authors (Z.Y., P.J.C.L.). M.A.G.H. and K.E.H.T. generated, expressed, and evaluated EABR constructs by Western blot and flow cytometry analysis. M.A.G.H., K.E.H.T., P.N.P.G., L.M.K., and K.N.S.

484 evaluated serum antibody responses from immunized mice by ELISA and
485 neutralization assays. Z.Y. performed cryo-electron tomography and interpreted
486 results. A.A.C. prepared S-mi3 immunogens for immunization studies in mice. W.J.M.
487 and P.J.C.L. prepared mRNA-LNP for immunization studies in mice.
488
489 **Competing interests**
490 M.A.G.H. and P.J.B. are inventors on a US patent application filed by the California
491 Institute of Technology that covers the EABR technology described in this work.
492 W.J.M. and P.J.C.L. are employees of Acuitas Therapeutics, a company developing
493 lipid nanoparticle delivery technology; P.J.C.L. holds equity in Acuitas Therapeutics.
494
495 **Data availability**
496 All data are available in the main text or the supplementary information. Materials are
497 available upon request to the corresponding authors with a signed material transfer
498 agreement. This work is licensed under a Creative Commons Attribution 4.0
499 International (CC BY 4.0) license, which permits unrestricted use, distribution, and
500 reproduction in any medium, provided the original work is properly cited. To view a
501 copy of this license, visit https://creativecommons.org/licenses/by/4.0/. This license
502 does not apply to figures/photos/artwork or other content included in the article that is
503 credited to a third party; obtain authorization from the rights holder before using such
504 material.
505
506

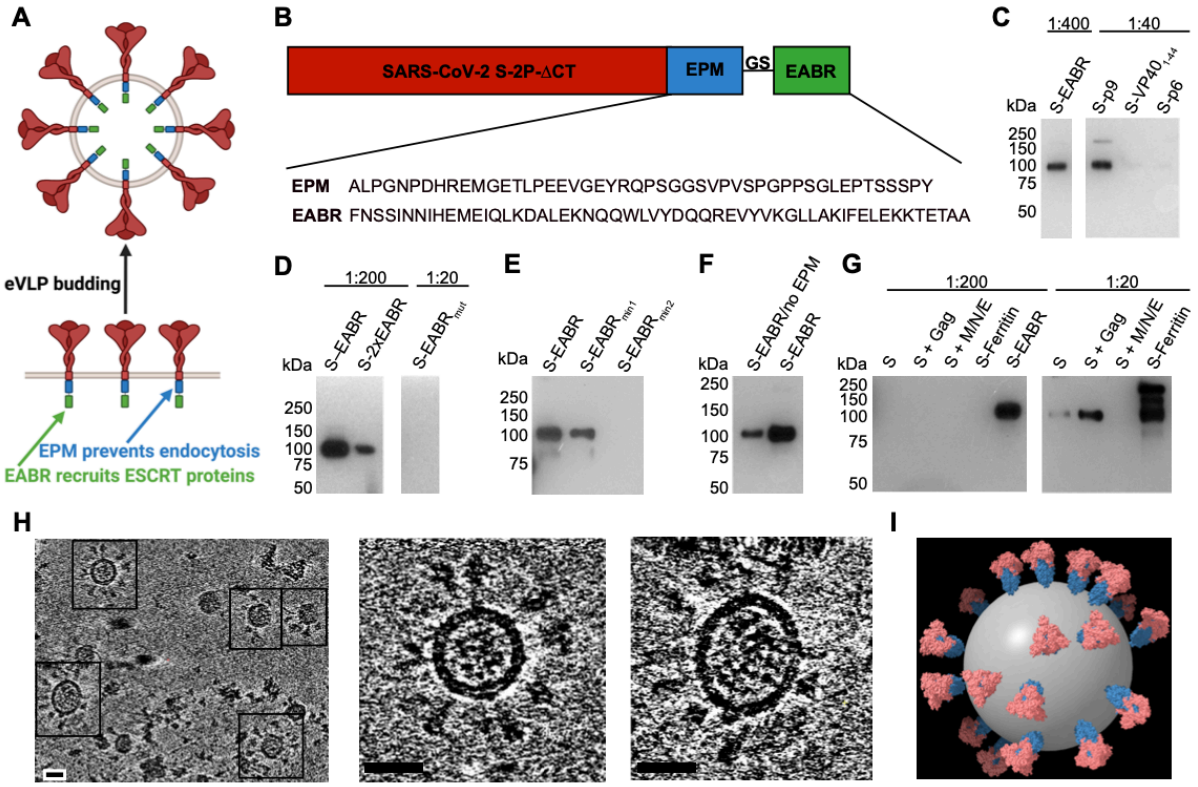

Figure 1 EABR insertion into the cytoplasmic tail of membrane proteins results in eVLP budding and release.

(A) Schematic of membrane-bound SARS-CoV-2 S proteins on the cell surface containing cytoplasmic tail EPM and EABR insertions that induce budding of an eVLP comprising a lipid bilayer with embedded S proteins.

(B) Sequence information for S-EABR construct. Top: The SARS-CoV-2 S protein (including a furin cleavage site, 2P stabilizing substitutions, the D614G substitution, and ΔCT, a cytoplasmic tail deletion) is fused to an EPM sequence, a $(Gly)_3Ser$ (GS) spacer, and an EABR sequence. EPM = Endocytosis prevention motif. GS = $(Gly)_3Ser$ linker. EABR = ESCRT- and ALIX-binding region. Bottom: EPM and EABR sequence information.

(C-G) Western blot analysis detecting SARS-CoV-2 S1 protein on eVLPs purified by ultracentrifugation on a 20% sucrose cushion from transfected Expi293F cell culture supernatants. (C) Cells were transfected with S-EABR, S-p9, S-VP40$_{1-44}$, or S-p6 constructs. The purified S-EABR eVLP sample was diluted 1:400 (left), while S-p9, S-VP40$_{1-44}$, and S-p6 samples were diluted 1:40 (right). Comparison of band intensities between lanes suggest that the S-EABR eVLP sample contained ~10-fold higher levels of S1 protein than the S-p9 sample and >10-fold higher levels than the S-VP40$_{1-44}$ and S-p6 samples. (D) Cells were transfected with S-EABR, S-2xEABR (left) or S-EABR$_{mut}$ constructs (right). Purified S-EABR and S-2xEABR eVLP samples were diluted 1:200, while the S-EABR$_{mut}$ sample was diluted 1:20. (E) Cells were transfected with S-EABR, S-EABR$_{min1}$, or S-EABR$_{min2}$ constructs. Purified eVLP samples were diluted 1:200. (F) Cells were transfected with S-EABR/no EPM or S-EABR constructs. Purified eVLP samples were diluted 1:200. (G) Cells were transfected to express S alone, S plus the HIV-1 Gag protein, S plus the SARS-CoV-2 M, N, and E proteins, an S-ferritin fusion protein, or S-EABR. Purified eVLP samples were diluted 1:200 (left) or 1:20 (right). Comparison of band intensities between lanes suggest that the S-EABR eVLP sample contained >10-fold higher levels of S1 protein than S alone, S plus Gag, and S plus M, N, E.

(H) Computationally-derived tomographic slices (8.1 nm) of S-EABR eVLPs derived from cryo-ET imaging of S-EABR eVLPs purified from transfected cell culture supernatants by ultracentrifugation on a 20% sucrose cushion and SEC. Left: Representative eVLPs are highlighted in boxes. Middle and right: Close-ups of individual eVLPs. Scale bars = 30 nm.

545 (I) Model of a representative S-EABR eVLP derived from a cryo-ET reconstruction
546 (Movie S1). Coordinates of an S trimer (PDB 6VXX) (Walls et al., 2020) were fit into
547 protruding density on the best resolved half of an eVLP and the remainder of the eVLP
548 was modeled assuming a similar distribution of trimers. The position of the lipid bilayer
549 is shown as a 55 nm gray sphere.
550

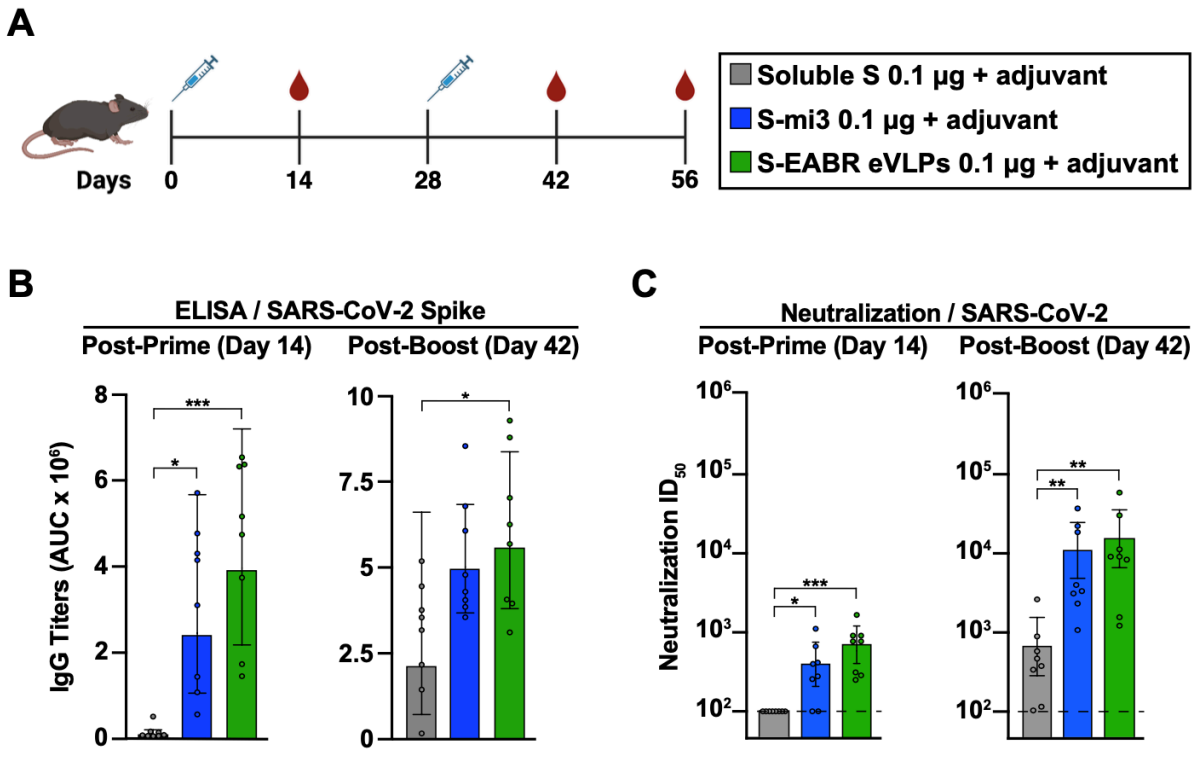

Figure 2 Purified S-EABR eVLPs induce potent antibody responses in mice.

(A) Immunization schedule. C57BL/6 mice were immunized with soluble S (purified S trimer) (gray), S-mi3 (S trimer ectodomains covalently attached to mi3, a 60-mer protein nanoparticle) (blue), or S-EABR eVLPs (green).

(B-C) ELISA and neutralization data from the indicated time points for antisera from individual mice (colored circles) presented as the geometric mean (bars) and standard deviation (horizontal lines). ELISA results are shown as area under the curve (AUC); neutralization results are shown as half-maximal inhibitory dilutions (ID_{50} values). Dashed horizontal lines correspond to the background values representing the limit of detection for neutralization assays. Significant differences between cohorts linked by horizontal lines are indicated by asterisks: $p<0.05$ = *, $p<0.01$ = **, $p<0.001$ = ***.

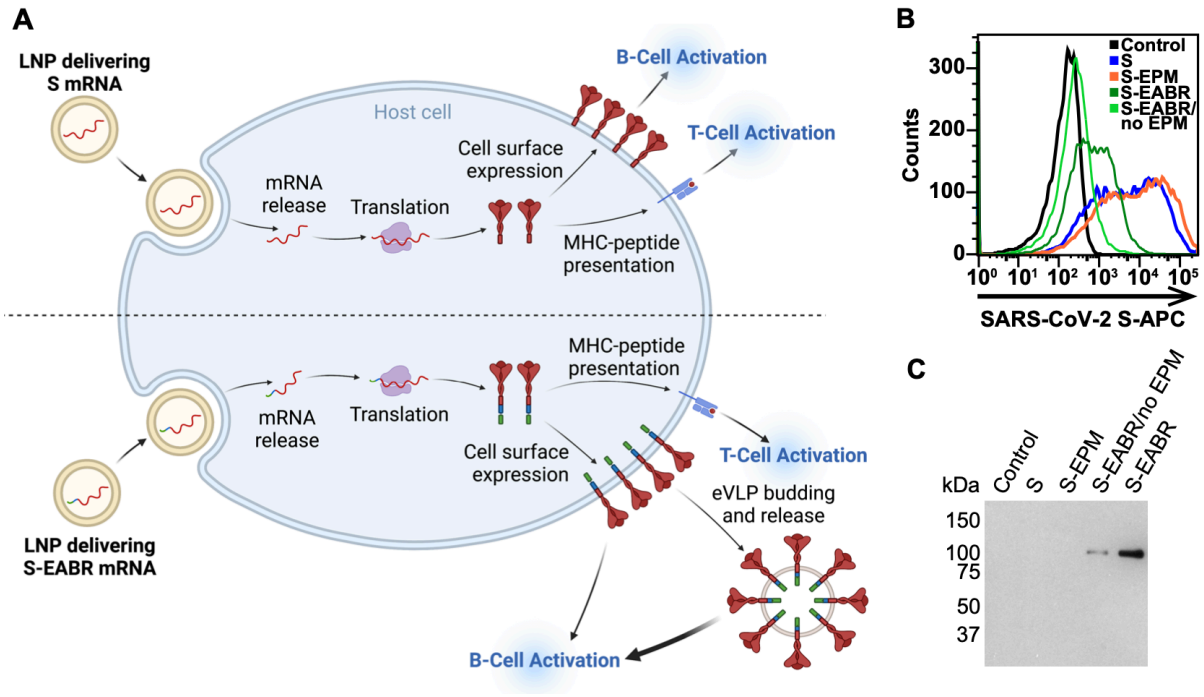

Figure 3 mRNA-mediated delivery of the S-EABR construct results in cell surface expression and eVLP assembly.

(A) Schematic comparison of mRNA-LNP delivery of S (as in COVID-19 mRNA vaccines) (top) versus delivery of an S-EABR construct (bottom). Both approaches generate S peptides displayed on class I MHC molecules for $CD8^+$ T cell recognition and result in presentation of S antigens on cell surfaces. The S-EABR approach also results in budding and release of eVLPs displaying S antigens.

(B) Flow cytometry analysis of SARS-CoV-2 S cell surface expression on HEK293T cells that were untransfected (black) or transfected with mRNAs encoding S (blue), S-EPM (orange), S-EABR (dark green), or S-EABR/no EPM (light green) constructs.

(C) Western blot analysis of eVLPs purified by ultracentrifugation on a 20% sucrose cushion from supernatants from the transfected cells in panel B. Purified eVLP samples were diluted 1:10.

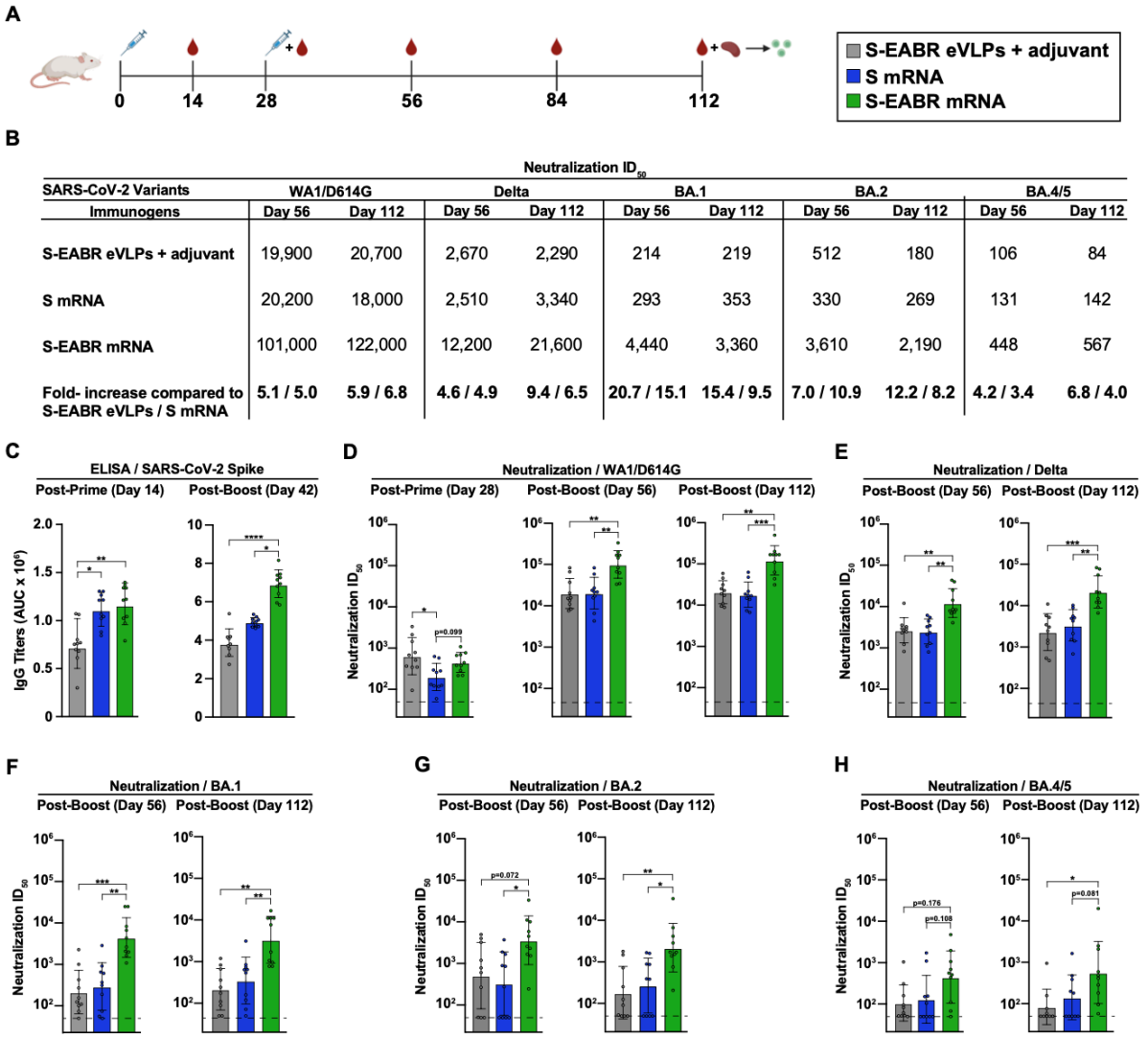

SARS-CoV-2 Variants	WA1/D614G		Delta		BA.1		BA.2		BA.4/5	
Immunogens	Day 56	Day 112	Day 56	Day 112	Day 56	Day 112	Day 56	Day 112	Day 56	Day 112
S-EABR eVLPs + adjuvant	19,900	20,700	2,670	2,290	214	219	512	180	106	84
S mRNA	20,200	18,000	2,510	3,340	293	353	330	269	131	142
S-EABR mRNA	101,000	122,000	12,200	21,600	4,440	3,360	3,610	2,190	448	567
Fold- increase compared to S-EABR eVLPs / S mRNA	5.1 / 5.0	5.9 / 6.8	4.6 / 4.9	9.4 / 6.5	20.7 / 15.1	15.4 / 9.5	7.0 / 10.9	12.2 / 8.2	4.2 / 3.4	6.8 / 4.0

Figure 4 mRNA-LNP encoding S-EABR eVLPs induce potent antibody responses in mice.

(A) Immunization schedule. BALB/c mice were immunized with purified S-EABR eVLPs (1 μg S protein) plus adjuvant (gray), 2 μg of mRNA-LNP encoding S (blue), or 2 μg of mRNA-LNP encoding S-EABR (green). On day 112, spleens were harvested from immunized mice for ELISpot analysis.

(B) Neutralization data from indicated time points for antisera presented as geometric mean half-maximal inhibitory dilution (ID_{50}) values against SARS-CoV-2 WA1/D614G, Delta, Omicron BA.1, Omicron BA.2, and Omicron BA.4/5 pseudoviruses. Bottom

horizontal row shows the fold increases for geometric mean ID_{50} values for mice that received S-EABR mRNA-LNP compared to mice that received purified S-EABR eVLPs or S mRNA-LNP.

(C) ELISA data from the indicated time points for antisera from individual mice (colored circles) presented as the geometric mean (bars) and standard deviation (horizontal lines). ELISAs evaluated binding of SARS-CoV-2 S trimers; results are shown as area under the curve (AUC).

(D-H) Neutralization data from the indicated time points for antisera from individual mice (colored circles) presented as the geometric mean (bars) and standard deviation (horizontal lines). Neutralization results against SARS-CoV-2 WA1/D614G (D), Delta (E), Omicron BA.1 (F), Omicron BA.2 (G), and Omicron BA.4/5 (H) pseudoviruses are shown as ID_{50} values. Dashed horizontal lines correspond to the background values representing the limit of detection for neutralization assays. Significant differences between cohorts linked by horizontal lines are indicated by asterisks: $p<0.05$ = *, $p<0.01$ = **, $p<0.001$ = ***, $p<0.0001$ = ****.

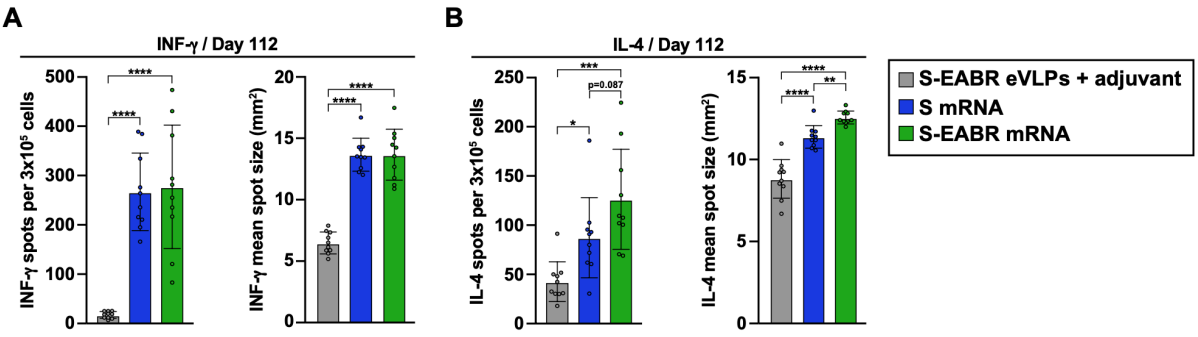

Figure 5 mRNA-LNP encoding S-EABR eVLPs induce potent T cell responses in mice.

(A-B) ELISpot assay data for SARS-CoV-2 S-specific INF-γ (A) and IL-4 (B) responses of splenocytes from BALB/c mice that were immunized with purified S-EABR eVLPs (1 µg S protein) plus adjuvant (gray), 2 µg of mRNA-LNP encoding S (blue), or 2 µg of mRNA-LNP encoding S-EABR (green). Results are shown as spots per $3x10^5$ cells (left) and mean spot sizes (right) for individual mice (colored circles) presented as the mean (bars) and standard deviation (horizontal lines). Significant differences between cohorts linked by horizontal lines are indicated by asterisks: $p<0.05$ = *, $p<0.01$ = **, $p<0.001$ = ***, $p<0.0001$ = ****.

627 **Supplemental Information**
628

629 **Title: ESCRT recruitment to mRNA-encoded SARS-CoV-2 spike induces virus-**
630 **like particles and enhanced antibody responses**

631

632 **Authors:** Magnus A. G. Hoffmann[1*], Zhi Yang[1‡], Kathryn E. Huey-Tubman[1],
633 Alexander A. Cohen[1], Priyanthi N. P. Gnanapragasam[1], Leesa M. Nakatomi[1], Kaya
634 N. Storm[1], Woohyun J. Moon[2], Paulo J.C. Lin[2], Pamela J. Bjorkman[1*]

635

636 **Affiliations:**
637 [1]Division of Biology and Biological Engineering, California Institute of Technology,
638 Pasadena, CA 91125, USA
639 [2]Acuitas Therapeutics, Vancouver, BC, V6T 1Z3, CANADA
640 ‡Present address: Department of Molecular and Cell Biology, University of California,
641 Berkeley, CA 94720, USA

642

643 [*]To whom correspondence should be addressed: Email: mhoffman@caltech.edu,
644 bjorkman@caltech.edu

645

646

Methods

Design of EABR constructs

The EABR domain (residues 160-217) of the human CEP55 protein was fused to the C-terminus of the SARS-CoV-2 S protein (WA1/D614G) separated by a 4-residue $(Gly)_3Ser$ (GS) linker to generate S-EABR/no EPM. This construct contained the native furin cleavage site, 2P stabilizing mutations (Pallesen et al., 2017), and the C-terminal 21 residues were truncated to remove an ER-retention signal (McBride et al., 2007). The S-EABR construct was generated by inserting residues 243-290 of mouse FcgRII-B1 upstream of the 4-residue GS linker and the EABR domain. The S-$EABR_{min1}$ and S-$EABR_{min2}$ constructs encoded residues 170-217 and 170-208 of CEP55, respectively. EABR constructs were also generated for HIV-1 Env_{YU2} and human CCR5. S-p6, S-$VP40_{1-44}$, and S-p9 were generated by replacing the EABR domain gene with sequences encoding HIV-1 p6 (isolate HXB2), EBOV VP40 (residues 1-44; Zaire EBOV), and EIAV p9 (strain Wyoming), respectively. The S-ferritin construct was designed as described (Powell et al., 2021) by fusing genes encoding the ectodomain of SARS-CoV-2 S WA1/D614G containing a furin cleavage site and 2P mutations, and *Helicobacter pylori* ferritin, separated by a 3-residue Ser-Gly-Gly linker. All constructs were cloned into the p3bNC expression plasmid.

Production of EABR eVLPs

EABR eVLPs were generated by transfecting Expi293F cells (Gibco) cultured in Expi293F expression media (Gibco) on an orbital shaker at 37°C and 8% CO_2. Gag-based eVLPs were produced by co-transfecting Expi293F cells with a plasmid expressing Rev-independent HIV-1 Gag-Pol (pHDM-Hgpm2 plasmid; PlasmID Repository, Harvard Medical School) and SARS-CoV-2 S, HIV-1 Env_{YU2}, or CCR5,

672 respectively, at a ratio of 1:1. SARS-CoV-2 M/N/E-based eVLPs were produced by
673 co-transfecting Expi293F cells with plasmids expressing the SARS-CoV-2 M, N, E,
674 and S proteins at a ratio of 1:1:1:1. To enable interactions between M, N, E, and S,
675 we transfected full-length S with an untruncated cytoplasmic domain. 72 hours post-
676 transfection, cells were centrifuged at 400 x g for 10 min, supernatants were passed
677 through a 0.45 µm syringe filter and concentrated using Amicon Ultra-15 centrifugal
678 filters with 100 kDa molecular weight cut-off (Millipore). eVLPs were purified by
679 ultracentrifugation at 50,000 rpm (135,000 x g) for 2 hours at 4°C using a TLA100.3
680 rotor and a Optima^{TM} TLX ultracentrifuge (Beckman Coulter) on a 20% w/v sucrose
681 cushion. Supernatants were removed and pellets were re-suspended in 200 µL sterile
682 PBS at 4°C overnight. To remove residual cell debris, samples were centrifuged at
683 10,000 x g for 10 min and supernatants were collected. For in vivo studies and cryo-
684 ET, eVLPs were further purified by SEC using a Superose 6 10/300 column (GE
685 Healthcare) equilibrated with PBS. Peak fractions corresponding to S-EABR eVLPs
686 were combined and concentrated to 250-500 µL in Amicon Ultra-4 centrifugal filters
687 with 100 kDa molecular weight cut-off. Samples were aliquoted and stored at -20°C.
688
689 **Protein expression**
690 Soluble SARS-CoV-2 S-6P trimers (WA1/D614G) (Hsieh et al., 2020) and RBDs were
691 expressed as described (Cohen et al., 2022; Wang et al., 2022). Briefly, Avi/His-
692 tagged proteins were purified from transiently-transfected Expi293F cells (Gibco) by
693 nickel affinity chromatography and SEC (Barnes et al., 2020; Cohen et al., 2022; Wang
694 et al., 2022). Peak fractions corresponding to S-6P or RBD proteins were pooled,
695 concentrated, and stored at 4ºC. Biotinylated proteins for ELISAs were generated by
696 co-transfection of Avi/His-tagged S-6P and RBD constructs with a plasmid encoding

an endoplasmic reticulum-directed BirA enzyme (kind gift from Michael Anaya, Caltech). S-6P constructs with a C-terminal SpyTag003 tag (Keeble et al., 2019) were expressed for covalent coupling to a 60-mer protein nanoparticle (SpyCatcher003-mi3) using the SpyCatcher-SpyTag system (Brune et al., 2016; Zakeri et al., 2012).

Preparation of SpyCatcher003-mi3 nanoparticles

SpyCatcher003-mi3 (Cohen et al., 2021) displaying SpyTagged SARS-CoV-2 S-6P trimers were prepared as described (Cohen et al., 2021; Cohen et al., 2022). Briefly, SpyCatcher003-mi3 subunits with N-terminal 6xHis tags were expressed in BL21 (DE3)-RIPL *E. coli* (Agilent). Bacterial cell pellets were lysed using a cell disruptor in the presence of 2.0 mM PMSF (Sigma). Lysates were centrifuged at 21,000 x g for 30 min, and supernatants were collected and filtered through a 0.2 µm filter. SpyCatcher003-mi3 was purified by Ni-NTA chromatography using a pre-packed HisTrap™ HP column (GE Healthcare), concentrated in Amicon Ultra-15 centrifugal filters with 30 kDa molecular weight cut-off (Millipore), and purified by SEC on a HiLoad 16/600 Superdex 200 column (GE Healthcare) equilibrated with TBS. S-mi3 nanoparticles were generated by incubating purified SpyCatcher003-mi3 with a 3-fold molar excess of purified SpyTagged S-6P trimer overnight at 4ºC in TBS. Conjugated S-mi3 nanoparticles were separated from uncoupled S-6P trimers by SEC using a Superose 6 10/300 column (GE Healthcare) equilibrated with PBS. Fractions corresponding to conjugated S-mi3 were identified by sodium dodecyl sulfate polyacrylamide gel electrophoresis (SDS-PAGE) and pooled.

722 **Western blot analysis**

723 The presence of SARS-CoV-2 S, HIV-1 Env_{YU2}, and CCR5 on purified eVLPs was
724 detected by Western blot analysis. Samples were diluted in SDS-PAGE loading buffer
725 under reducing conditions, separated by SDS-PAGE, and transferred to nitrocellulose
726 membranes (0.2 µm) (GE Healthcare). The following antibodies were used for
727 detecting SARS-CoV-2 S, HIV-1 Env_{YU2}, and CCR5: rabbit anti-SARS-CoV-2 S1
728 protein (PA5-81795; ThermoFisher) at 1:2,500, the human anti-HIV-1 Env broadly
729 neutralizing antibody 10-1074 (Mouquet et al., 2012) (expressed in-house) at
730 1:10,000, rat anti-CCR5 (ab111300; Abcam) at 1:2,000, HRP-conjugated mouse anti-
731 rabbit IgG (211-032-171; Jackson ImmunoResearch) at 1:10,000, HRP-conjugated
732 goat anti-human IgG (2014-05; Southern Biotech) at 1:8,000, and HRP-conjugated
733 mouse anti-rat IgG (3065-05; Southern Biotech) at 1:10,000. Protein bands were
734 visualized using ECL Prime Western Blotting Detection Reagent (GE Healthcare).
735
736 For in vivo studies, the amount of SARS-CoV-2 S on S-EABR eVLPs was determined
737 by quantitative Western blot analysis. Various dilutions of SEC-purified S-EABR eVLP
738 samples and known amounts of soluble SARS-CoV-2 S1 protein (Sino Biological)
739 were separated by SDS-PAGE and transferred to nitrocellulose membranes (GE
740 Healthcare). SARS-CoV-2 S was detected as described above. Band intensities of the
741 SARS-CoV-2 S1 standards and S-EABR eVLP sample dilutions were measured using
742 ImageJ to determine S concentrations. The S1 protein concentrations determined for
743 S-EABR samples were multiplied by a factor of 1.8 to account for the difference in
744 molecular weight between S1 and the full-length S protein.
745
746

747 **Cryo-ET of S-EABR eVLPs**

748 SEC-purified S-EABR eVLPs were prepared on grids for cryo-ET using a Mark IV
749 Vitrobot (ThermoFisher Scientific) operated at 21°C and 100% humidity. 2.5 µL of
750 sample was mixed with 0.4 µL of 10 nm fiducial gold beads (Sigma-Aldrich) and
751 applied to 300-mesh Quantifoil R2/2 grids, blotted for 3.5 s, and then plunge-frozen in
752 liquid ethane cooled by liquid nitrogen. Image collections were performed on a 300 kV
753 Titan Krios transmission electron microscope (ThermoFisher Scientific) operating at a
754 nominal 42,000x magnification. Tilt series were collected on a K3 direct electron
755 detector (Gatan) with a pixel size of 2.15 Å•pixel^{-1} using SerialEM software
756 (Mastronarde, 2005). The defocus range was set to -5 to -8 µm and a total of 120 e^- •
757 Å^{-2} per tilt series. Images were collected using a dose-symmetric scheme (Hagen et
758 al., 2017) ranging from -60° to 60° with 3° intervals. Tomograms were aligned and
759 reconstructed using IMOD (Mastronarde and Held, 2017).
760
761 To build a model of an S-EABR eVLP, coordinates of a SARS-CoV-2 S trimer (PDB
762 6VXX) were fit into spike densities in the reconstructed tomograms using ChimeraX
763 (Goddard et al., 2018). Positions and orientations of the S protein were adjusted in a
764 hemisphere of the eVLP in which the spike density was of higher quality. A 55 nm
765 sphere was adapted from a cellPACK model (cellPACK ID: HIV-1_0.1.6_6) (Johnson
766 et al., 2015; Johnson et al., 2014) and added to the model to represent the eVLP
767 membrane surface.
768
769 **Neutralization assays**
770 Lentivirus-based SARS-CoV-2 pseudoviruses were generated as described
771 (Crawford et al., 2020; Robbiani et al., 2020) using S proteins from the WA1/D614G,

772 Delta, Omicron BA.1, Omicron BA.2, and Omicron BA.4/5 variants in which the C-
773 terminal 21 residues of the S protein cytoplasmic tails were removed (Crawford et al.,
774 2020). Serum samples from immunized mice were heat-inactivated for 30 min at 56ºC.
775 Three-fold serial dilutions of heat-inactivated samples were incubated with
776 pseudoviruses for 1 hour at 37ºC, followed by addition of the serum-virus mixtures to
777 pre-seeded HEK293T-ACE2 target cells. After 48-hour incubation at 37ºC, BriteLite
778 Plus substrate (Perkin Elmer) was added and luminescence was measured. Half-
779 maximal inhibitory dilutions (ID_{50}s) were calculated using 4-parameter non-linear
780 regression analysis in AntibodyDatabase (West et al., 2013) and ID_{50} values were
781 rounded to three significant figures.
782
783 $PRNT_{50}$ (50% plaque reduction neutralization test) assays with authentic SARS-CoV-
784 2 virus were performed in a biosafety level 3 facility at BIOQUAL, Inc. (Rockville, MD)
785 as described (Haun et al., 2020). Mouse sera from day 56 post-immunization were
786 diluted 1:20 and then 3-fold serially diluted in culture media (DMEM + 10% FBS +
787 Gentamicin). The diluted samples were incubated with 30 plaque-forming units of wild-
788 type SARS-CoV-2 (USA-WA1/2020, BEI Resources NR-52281; Beta variant, Isolate
789 hCoV-19/South Africa/KRISP-K005325/2020, BEI Resources NR-54009; Delta
790 variant, isolate hCoV-19/USA/MD-HP05647/2021 BEI Resources NR-55674) for 1
791 hour at 37ºC. Samples were then added to a confluent monolayer of Vero/TMPRSS2
792 cells in 24-well plates for 1 hour at 37ºC in 5% CO_2. 1 mL of culture media with 0.5%
793 methylcellulose was added to each well and plates were incubated for 3 days at 37ºC
794 in 5% CO_2. Plates were fixed with ice cold methanol at -20ºC for 30 min. Methanol
795 was discarded and plates were stained with 0.2% crystal violet for 30 min at room
796 temperature. Plates were washed once with water and plaques in each well were

797 counted. $TCID_{50}$ values were calculated using the Reed-Muench formula (Reed and
798 Muench, 1938).
799
800 **ELISAs**
801 Pre-blocked streptavidin-coated Nunc® MaxiSorp™ 384-well plates (Sigma) were
802 coated with 5 µg/mL biotinylated S-6P or RBD proteins in Tris-buffered saline with
803 0.1% Tween 20 (TBS-T) and 3% bovine serum albumin (BSA) for 1 hour at room
804 temperature. Serum samples from immunized mice were diluted 1:100, 4-fold serially
805 diluted in TBS-T/3% BSA, and then added to plates. After a 3-hour incubation at room
806 temperature, plates were washed with TBS-T using an automated plate washer. HRP-
807 conjugated goat anti-mouse IgG (715-035-150; Jackson ImmunoResearch) was
808 diluted 1:100,000 in TBS-T/3% BSA and added to plates for 1 hour at room
809 temperature. After washing with TBS-T, plates were developed using SuperSignal™
810 ELISA Femto Maximal Signal Substrate (ThermoFisher) and absorbance was
811 measured at 425 nm. Area under the curve (AUC) calculations for binding curves were
812 performed using GraphPad Prism 9.3.1 assuming a one-site binding model with a Hill
813 coefficient as described (Cohen et al., 2021).
814
815 **mRNA synthesis**
816 Codon-optimized mRNAs encoding SARS-CoV-2 S, S-EPM, S-EABR/no EPM, and
817 S-EABR constructs were synthesized by RNAcore
818 (https://www.houstonmethodist.org/research-cores/rnacore/) using proprietary
819 manufacturing protocols. mRNAs were generated by T7 RNA polymerase-mediated
820 in vitro transcription reactions using DNA templates containing the immunogen open
821 reading frame flanked by 5′ untranslated region (UTR) and 3′ UTR sequences and

terminated by an encoded polyA tail. CleanCap 5' cap structures (TriLink) were incorporated into the 5′ end co-transcriptionally. Uridine was completely replaced with N1-methyl-pseudouridine to reduce immunogenicity (Kariko et al., 2008). mRNAs were purified by oligo-dT affinity purification and high-performance liquid chromatography (HPLC) to remove double-stranded RNA contaminants (Kariko et al., 2011). Purified mRNAs were stored at –80 °C.

mRNA transfections

For mRNA transfections, 10^6 HEK293T cells were seeded in 6-well plates. After 24 hours, cells were transfected with 2 µg mRNA encoding SARS-CoV-2 S, S-EPM, S-EABR/no EPM, or S-EABR constructs using Lipofectamine™ MessengerMax™ transfection reagent (ThermoFisher). 48 hours post-transfection, supernatants were collected and purified for Western blot analysis. Cells were gently detached by pipetting and resuspended in 500 µL PBS. 100 µL were transferred into Eppendorf tubes for flow cytometry analysis of S cell surface expression. Cells were stained with the SARS-CoV-2 antibody C119 (Robbiani et al., 2020) at 5 µg/mL in PBS+ (PBS supplemented with 2% FBS) for 30 min at room temperature in the dark. After two washes in PBS+, samples were stained with an Alexa Fluor® 647-conjugated anti-human IgG secondary antibody (A21445; Life Technologies) at a 1:2,000 dilution in PBS+ for 30 min at room temperature in the dark. After two washes in PBS+, cells were resuspended in PBS+ and analyzed by flow cytometry (MACSQuant, Miltenyi Biotec). Results were plotted using FlowJo 10.5.3 software.

847 **LNP encapsulation of mRNAs**

848 Purified N1-methyl-pseudouridine mRNA was formulated in LNP as previously
849 described (Pardi et al., 2015). In brief, 1,2-distearoyl-*sn*-glycero-3-phosphocholine,
850 cholesterol, a PEG lipid, and an ionizable cationic lipid dissolved in ethanol were
851 rapidly mixed with an aqueous acidic solution containing mRNA using an in-line mixer.
852 The ionizable lipid and LNP composition are described in the international patent
853 application WO2017075531(2017). The post in-line solution was dialyzed with PBS
854 to remove the ethanol and displace the acidic solution. Subsequently, LNP was
855 measured for size (60-65 nm) and polydispersity (PDI < 0.075) by dynamic light
856 scattering (Malvern Nano ZS Zetasizer). Encapsulation efficiencies were >97% as
857 measured by the Quant-iT Ribogreen Assay (Life Technologies).

858

859 **Immunizations**

860 All animal procedures were performed in accordance with IACUC-approved protocols.
861 7-8 week-old female C57BL/6 or BALB/c mice (Charles River Laboratories) were used
862 for immunization experiments with cohorts of 8-10 animals per group. 0.1 μg of protein-
863 based immunogens, including soluble S trimer, S-mi3, and purified S-EABR eVLPs,
864 were administered to C57BL/6 mice by subcutaneous (SC) injections on days 0 and
865 28 in the presence of Sigma adjuvant system (Sigma). 2 μg of S and S-EABR mRNA-
866 LNP were administered to BALB/c mice by intramuscular (IM) injections on days 0 and
867 28. To compare mRNA- and protein-based immunogens, 1 μg purified S-EABR eVLPs
868 were administered IM in the presence of 50% v/v AddaVax^{TM} adjuvant (Invivogen).
869 Serum samples for ELISAs and neutralization assays were obtained on indicated
870 days.

871

872 **ELISpot assays**

873 Animals were euthanized on day 112 and spleens were collected. Spleens were
874 homogenized using a gentleMACS Octo Dissociator (Miltenyi Biotec). Cells were
875 passed through a 70 µm tissue screen, centrifuged at 1,500 rpm for 10 min, and
876 resuspended in CTL-Test™ media (ImmunoSpot) containing 1% GlutaMAX™ (Gibco)
877 for ELISpot analysis to evaluate T cell responses. A PepMix™ pool of 315 peptides
878 (15-mers with 11 amino acid overlap) derived from the SARS-CoV-2 S protein (JPT
879 Peptide Technologies) was added to mouse IFN-g/IL-4 double-color ELISpot plates
880 (ImmunoSpot) at a concentration of 2 µg/mL. 300,000 cells were added per well, and
881 plates were incubated at 37ºC for 24 hours. Biotinylated detection, streptavidin-
882 alkaline phosphatase (AP), and substrate solutions were added according to the
883 manufacturer's guidelines. Plates were gently rinsed with water three times to stop the
884 reactions. Plates were air-dried for two hours in a running laminar flow hood. The
885 number of spots and the mean spot sizes were quantified using a CTL ImmunoSpot
886 S6 Universal-V Analyzer (Immunospot).

887

888 **Statistical analysis**

889 Titer differences between immunized groups of mice for ELISAs and neutralization
890 assays were evaluated for statistical significance using the non-parametric Kruskal-
891 Wallis test followed by Dunn's multiple comparison post hoc test calculated using
892 Graphpad Prism 9.3.1. For ELISpot results, statistically significant differences
893 between immunized groups of mice were determined using analysis of variance
894 (ANOVA) test followed by Tukey's multiple comparison post hoc test calculated using
895 Graphpad Prism 9.3.1.

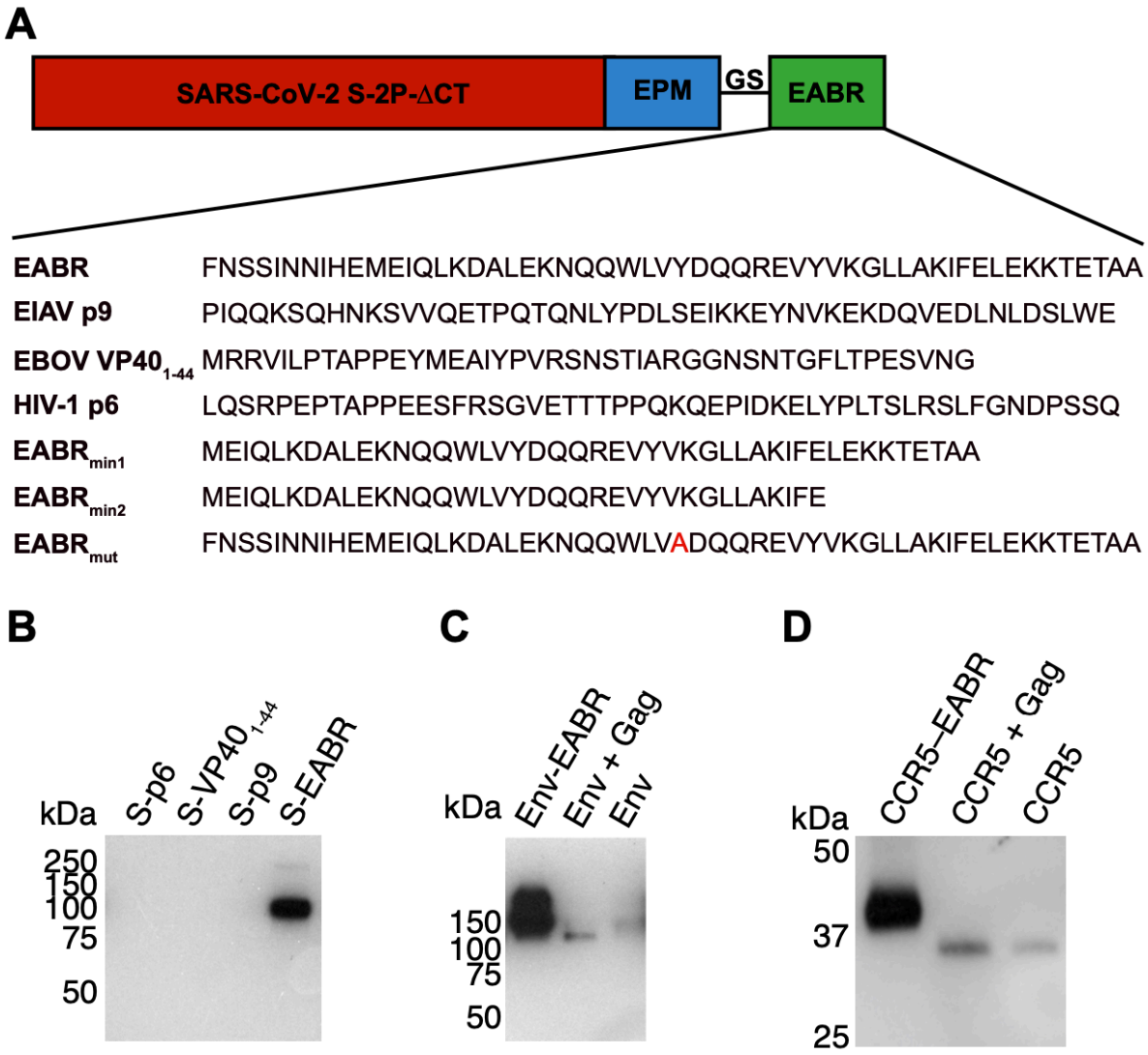

Figure S1 Comparison of EABR-related sequence insertions in the cytoplasmic tail of SARS-CoV-2 S, related to Figure 1.

(A) Top: Schematic of different S-EABR constructs that were compared for their ability to induce eVLP assembly. EPM = Endocytosis prevention motif. GS = $(Gly)_3Ser$ linker. EABR = ESCRT- and ALIX-binding region. Bottom: Amino acid sequences of EABR portion of different constructs.

(B) Western blot analysis of SARS-CoV-2 S1 protein levels on eVLPs purified by ultracentrifugation on a 20% sucrose cushion from transfected Expi293F cell culture

906 supernatants. Cells were transfected with S-p6, S-VP40$_{1-44}$, S-p9, or S-EABR
907 constructs. Purified eVLP samples were diluted 1:400.
908
909 (C) Western blot analysis comparing HIV-1 Env$_{YU2}$ levels in eVLP samples purified
910 from transfected Expi293F cell culture supernatants. Cells were transfected with
911 plasmids encoding Env-EABR, Env plus HIV-1 Gag, or Env alone. Purified eVLP
912 samples were diluted 1:200.
913
914 (D) Western blot analysis comparing CCR5 levels in eVLP samples purified from
915 transfected Expi293F cell culture supernatants. Cells were transfected with plasmids
916 encoding CCR5-EABR, CCR5 plus HIV-1 Gag, or CCR5 alone. Purified eVLP
917 samples were diluted 1:200. The migration difference between CCR5-EABR and
918 CCR5 is due to addition of the EABR sequence (~7 kDa) that increases its molecular
919 mass.

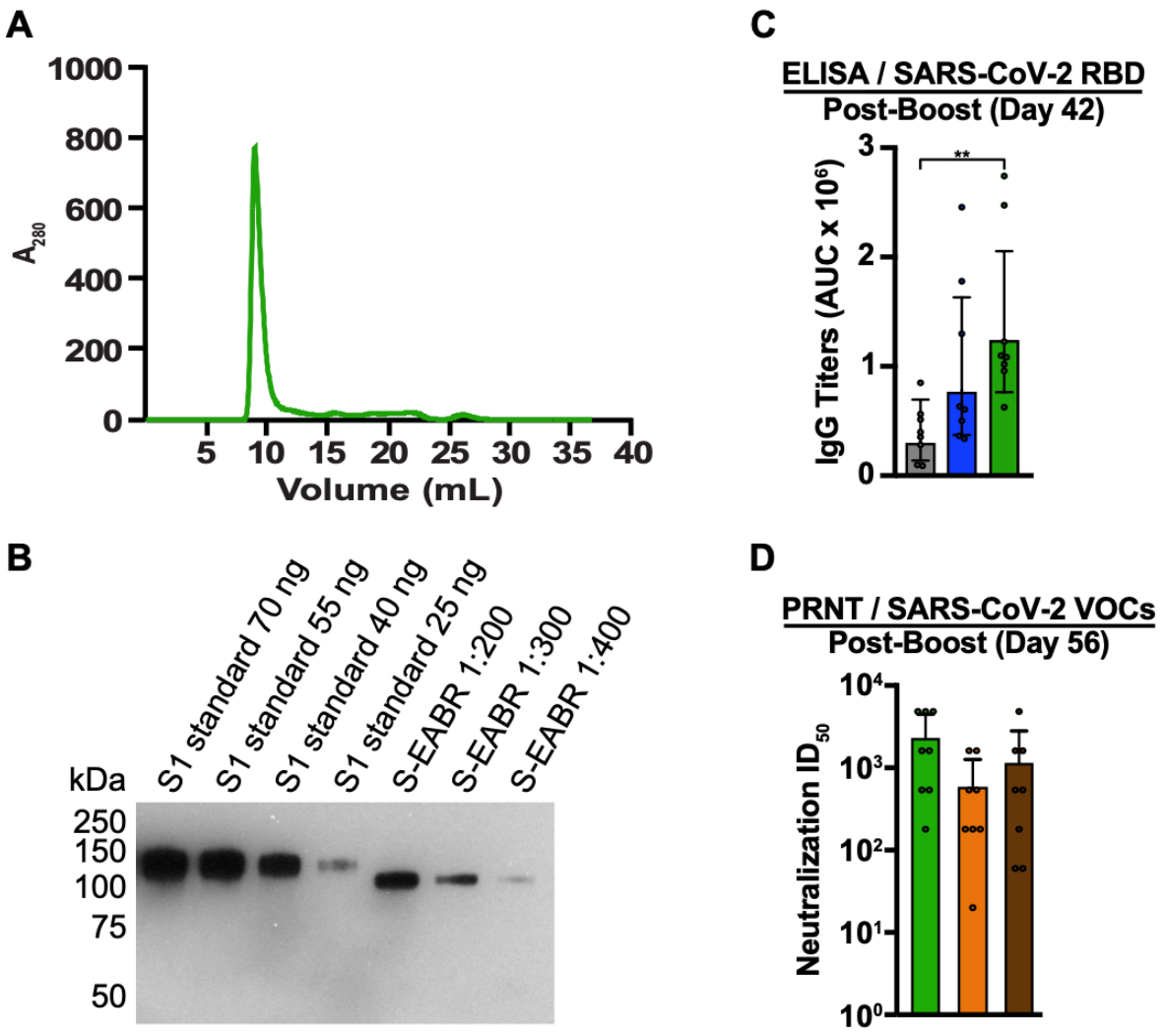

Figure S2 Purified S-EABR eVLPs induce potent antibody responses in mice, related to Figure 2.

(A) Size exclusion chromatogram of S-EABR eVLPs purified by ultracentrifugation on a 20% sucrose cushion.

(B) Quantitative Western blot comparing indicated amounts of SARS-CoV-2 S1 standards (lanes 1-4) and various dilutions of purified S-EABR eVLPs (lanes 5-7) to determine S protein concentrations in eVLP samples. The S1 standard protein (Sino Biological) was biotinylated and contained a polyhistidine tag, which resulted in a difference in apparent molecular weights for the S1 standards and the S-EABR

construct. Band intensities of S1 standards and S-EABR eVLP sample dilutions were measured using ImageJ to determine S concentrations.

(C) ELISA data from day 42 for antisera from individual mice (colored circles) immunized with soluble S (purified S trimer) (gray), S-mi3 (S trimer ectodomains covalently attached to mi3, a 60-mer protein nanoparticle) (blue), or S-EABR eVLPs (green). Results are shown as area under the curve (AUC) and presented as the geometric mean (bars) and standard deviation (horizontal lines). Significant differences between cohorts linked by horizontal lines are indicated by asterisks: $p<0.05$ = *, $p<0.01$ = **.

(D) PRNT assay results from day 56 for antisera from individual mice (colored circles) immunized with S-EABR eVLPs. Results against the SARS-CoV-2 WA1 (green), Beta (orange), and Delta (brown) variants are shown as $TCID_{50}$ values (Reed and Muench, 1938) and presented as the geometric mean (bars) and standard deviation (horizontal lines).

References

Alberts, B., Johnson, A., Lewis, J., Raff, M., Roberts, K.E., and Walter, P. (2002). Molecular Biology of the Cell, 4th ed. http://onlinelibrary.wiley.com/doi/10.1002/bmb.2003.494031049999/full (New York: Garland Science/Taylor & Francis LLC).

Baden, L.R., El Sahly, H.M., Essink, B., Kotloff, K., Frey, S., Novak, R., Diemert, D., Spector, S.A., Rouphael, N., Creech, C.B., *et al.* (2021). Efficacy and Safety of the mRNA-1273 SARS-CoV-2 Vaccine. N Engl J Med *384*, 403-416.

Barnes, C.O., Jette, C.A., Abernathy, M.E., Dam, K.-M.A., Esswein, S.R., Gristick, H.B., Malyutin, A.G., Sharaf, N.G., Huey-Tubman, K.E., Lee, Y.E., *et al.* (2020). SARS-CoV-2 neutralizing antibody structures inform therapeutic strategies. Nature *588*, 682-687.

Barouch, D.H. (2022). Covid-19 Vaccines - Immunity, Variants, Boosters. N Engl J Med *387*, 1011-1020.

Brune, K.D., Leneghan, D.B., Brian, I.J., Ishizuka, A.S., Bachmann, M.F., Draper, S.J., Biswas, S., and Howarth, M. (2016). Plug-and-Display: decoration of Virus-Like Particles via isopeptide bonds for modular immunization. Scientific reports *6*, 19234.

Chen, R.E., Zhang, X., Case, J.B., Winkler, E.S., Liu, Y., VanBlargan, L.A., Liu, J., Errico, J.M., Xie, X., Suryadevara, N., *et al.* (2021). Resistance of SARS-CoV-2 variants to neutralization by monoclonal and serum-derived polyclonal antibodies. Nat Med 10.1038/s41591-021-01294-w.

Chen, Y., Zhao, X., Zhou, H., Zhu, H., Jiang, S., and Wang, P. (2022). Broadly neutralizing antibodies to SARS-CoV-2 and other human coronaviruses. Nat Rev Immunol 10.1038/s41577-022-00784-3.

Cohen, A.A., Gnanapragasam, P.N.P., Lee, Y.E., Hoffman, P.R., Ou, S., Kakutani, L.M., Keeffe, J.R., Wu, H.J., Howarth, M., West, A.P., *et al.* (2021). Mosaic nanoparticles elicit cross-reactive immune responses to zoonotic coronaviruses in mice. Science *371*, 735-741.

Cohen, A.A., van Doremalen, N., Greaney, A.J., Andersen, H., Sharma, A., Starr, T.N., Keeffe, J.R., Fan, C., Schulz, J.E., Gnanapragasam, P.N.P., *et al.* (2022). Mosaic RBD nanoparticles protect against challenge by diverse sarbecoviruses in animal models. Science *377*, eabq0839.

Corbett, K.S., Edwards, D.K., Leist, S.R., Abiona, O.M., Boyoglu-Barnum, S., Gillespie, R.A., Himansu, S., Schafer, A., Ziwawo, C.T., DiPiazza, A.T., *et al.* (2020). SARS-CoV-2 mRNA vaccine design enabled by prototype pathogen preparedness. Nature *586*, 567-571.

Cox, M.M., and Hollister, J.R. (2009). FluBlok, a next generation influenza vaccine manufactured in insect cells. Biologicals *37*, 182-189.

Crawford, K.H.D., Eguia, R., Dingens, A.S., Loes, A.N., Malone, K.D., Wolf, C.R., Chu, H.Y., Tortorici, M.A., Veesler, D., Murphy, M., *et al.* (2020). Protocol and Reagents for Pseudotyping Lentiviral Particles with SARS-CoV-2 Spike Protein for Neutralization Assays. Viruses *12*.

Fisher, R.D., Chung, H.Y., Zhai, Q., Robinson, H., Sundquist, W.I., and Hill, C.P. (2007). Structural and biochemical studies of ALIX/AIP1 and its role in retrovirus budding. Cell *128*, 841-852.

Fujii, K., Munshi, U.M., Ablan, S.D., Demirov, D.G., Soheilian, F., Nagashima, K., Stephen, A.G., Fisher, R.J., and Freed, E.O. (2009). Functional role of Alix in HIV-1 replication. Virology *391*, 284-292.

Goddard, T.D., Huang, C.C., Meng, E.C., Pettersen, E.F., Couch, G.S., Morris, J.H., and Ferrin, T.E. (2018). UCSF ChimeraX: Meeting modern challenges in visualization and analysis. Protein Sci *27*, 14-25.

Gruell, H., Vanshylla, K., Tober-Lau, P., Hillus, D., Schommers, P., Lehmann, C., Kurth, F., Sander, L.E., and Klein, F. (2022). mRNA booster immunization elicits potent neutralizing serum activity against the SARS-CoV-2 Omicron variant. Nat Med *28*, 477-480.

Hachmann, N.P., Miller, J., Collier, A.Y., Ventura, J.D., Yu, J., Rowe, M., Bondzie, E.A., Powers, O., Surve, N., Hall, K.*, et al.* (2022). Neutralization Escape by SARS-CoV-2 Omicron Subvariants BA.2.12.1, BA.4, and BA.5. N Engl J Med *387*, 86-88.

Hagen, W.J.H., Wan, W., and Briggs, J.A.G. (2017). Implementation of a cryo-electron tomography tilt-scheme optimized for high resolution subtomogram averaging. J Struct Biol *197*, 191-198.

Haun, B.K., Lai, C.Y., Williams, C.A., Wong, T.A.S., Lieberman, M.M., Pessaint, L., Andersen, H., and Lehrer, A.T. (2020). CoVaccine HT Adjuvant Potentiates Robust Immune Responses to Recombinant SARS-CoV-2 Spike S1 Immunization. Front Immunol *11*, 599587.

Heath, P.T., Galiza, E.P., Baxter, D.N., Boffito, M., Browne, D., Burns, F., Chadwick, D.R., Clark, R., Cosgrove, C., Galloway, J.*, et al.* (2021). Safety and Efficacy of NVX-CoV2373 Covid-19 Vaccine. N Engl J Med *385*, 1172-1183.

Hoffmann, M.A.G., Bar-On, Y., Yang, Z., Gristick, H.B., Gnanapragasam, P.N.P., Vielmetter, J., Nussenzweig, M.C., and Bjorkman, P.J. (2020). Nanoparticles presenting clusters of CD4 expose a universal vulnerability of HIV-1 by mimicking target cells. Proc Natl Acad Sci U S A *117*, 18719-18728.

Hogan, M.J., and Pardi, N. (2022). mRNA Vaccines in the COVID-19 Pandemic and Beyond. Annu Rev Med *73*, 17-39.

Hsieh, C.L., Goldsmith, J.A., Schaub, J.M., DiVenere, A.M., Kuo, H.C., Javanmardi, K., Le, K.C., Wrapp, D., Lee, A.G., Liu, Y.*, et al.* (2020). Structure-based design of prefusion-stabilized SARS-CoV-2 spikes. Science *369*, 1501-1505.

Johnson, G.T., Autin, L., Al-Alusi, M., Goodsell, D.S., Sanner, M.F., and Olson, A.J. (2015). cellPACK: a virtual mesoscope to model and visualize structural systems biology. Nat Methods *12*, 85-91.

Johnson, G.T., Goodsell, D.S., Autin, L., Forli, S., Sanner, M.F., and Olson, A.J. (2014). 3D molecular models of whole HIV-1 virions generated with cellPACK. Faraday Discuss *169*, 23-44.

Joyce, M.G., Chen, W.H., Sankhala, R.S., Hajduczki, A., Thomas, P.V., Choe, M., Martinez, E.J., Chang, W.C., Peterson, C.E., Morrison, E.B.*, et al.* (2021). SARS-CoV-2 ferritin nanoparticle vaccines elicit broad SARS coronavirus immunogenicity. Cell reports *37*, 110143.

Karbiener, M., Farcet, M.R., Zollner, A., Masuda, T., Mori, M., Moschen, A.R., and Kreil, T.R. (2022). Calibrated comparison of SARS-CoV-2 neutralizing antibody levels in response to protein-, mRNA-, and vector-based COVID-19 vaccines. NPJ Vaccines *7*, 22.

Kariko, K., Muramatsu, H., Ludwig, J., and Weissman, D. (2011). Generating the optimal mRNA for therapy: HPLC purification eliminates immune activation and improves translation of nucleoside-modified, protein-encoding mRNA. Nucleic Acids Res *39*, e142.

Kariko, K., Muramatsu, H., Welsh, F.A., Ludwig, J., Kato, H., Akira, S., and Weissman, D. (2008). Incorporation of pseudouridine into mRNA yields superior

nonimmunogenic vector with increased translational capacity and biological stability. Mol Ther *16*, 1833-1840.
Ke, Z., Oton, J., Qu, K., Cortese, M., Zila, V., McKeane, L., Nakane, T., Zivanov, J., Neufeldt, C.J., Cerikan, B.*, et al.* (2020). Structures and distributions of SARS-CoV-2 spike proteins on intact virions. Nature 10.1038/s41586-020-2665-2.
Keeble, A.H., Turkki, P., Stokes, S., Khairil Anuar, I.N.A., Rahikainen, R., Hytönen, V.P., and Howarth, M. (2019). Approaching infinite affinity through engineering of peptide–protein interaction. Proceedings of the National Academy of Sciences *116*, 26523-26533.
Keech, C., Albert, G., Cho, I., Robertson, A., Reed, P., Neal, S., Plested, J.S., Zhu, M., Cloney-Clark, S., Zhou, H.*, et al.* (2020). Phase 1-2 Trial of a SARS-CoV-2 Recombinant Spike Protein Nanoparticle Vaccine. N Engl J Med *383*, 2320-2332.
Kent, S.J., Khoury, D.S., Reynaldi, A., Juno, J.A., Wheatley, A.K., Stadler, E., John Wherry, E., Triccas, J., Sasson, S.C., Cromer, D.*, et al.* (2022). Disentangling the relative importance of T cell responses in COVID-19: leading actors or supporting cast? Nat Rev Immunol *22*, 387-397.
Khoury, D.S., Docken, S.S., Subbarao, K., Kent, S.J., Davenport, M.P., and Cromer, D. (2022). Predicting the efficacy of variant-modified COVID-19 vaccine boosters. medRxiv 10.1101/2022.08.25.22279237.
Kleanthous, H., Silverman, J.M., Makar, K.W., Yoon, I.K., Jackson, N., and Vaughn, D.W. (2021). Scientific rationale for developing potent RBD-based vaccines targeting COVID-19. NPJ Vaccines *6*, 128.
Korber, B., Fischer, W.M., Gnanakaran, S., Yoon, H., Theiler, J., Abfalterer, W., Hengartner, N., Giorgi, E.E., Bhattacharya, T., Foley, B.*, et al.* (2020). Tracking Changes in SARS-CoV-2 Spike: Evidence that D614G Increases Infectivity of the COVID-19 Virus. Cell *182*, 812-827.e819.
Kraft, J.C., Pham, M.N., Shehata, L., Brinkkemper, M., Boyoglu-Barnum, S., Sprouse, K.R., Walls, A.C., Cheng, S., Murphy, M., Pettie, D.*, et al.* (2022). Antigen- and scaffold-specific antibody responses to protein nanoparticle immunogens. Cell Rep Med *3*, 100780.
Lee, H.H., Elia, N., Ghirlando, R., Lippincott-Schwartz, J., and Hurley, J.H. (2008). Midbody targeting of the ESCRT machinery by a noncanonical coiled coil in CEP55. Science *322*, 576-580.
Lu, J., Lu, G., Tan, S., Xia, J., Xiong, H., Yu, X., Qi, Q., Yu, X., Li, L., Yu, H.*, et al.* (2020). A COVID-19 mRNA vaccine encoding SARS-CoV-2 virus-like particles induces a strong antiviral-like immune response in mice. Cell Res *30*, 936-939.
Madara, J.J., Han, Z., Ruthel, G., Freedman, B.D., and Harty, R.N. (2015). The multifunctional Ebola virus VP40 matrix protein is a promising therapeutic target. Future Virol *10*, 537-546.
Martins, S.A., Santos, J., Silva, R.D.M., Rosa, C., Cabo Verde, S., Correia, J.D.G., and Melo, R. (2022). How promising are HIV-1-based virus-like particles for medical applications. Front Cell Infect Microbiol *12*, 997875.
Mastronarde, D.N. (2005). Automated electron microscope tomography using robust prediction of specimen movements. J Struct Biol *152*, 36-51.
Mastronarde, D.N., and Held, S.R. (2017). Automated tilt series alignment and tomographic reconstruction in IMOD. J Struct Biol *197*, 102-113.
McBride, C.E., Li, J., and Machamer, C.E. (2007). The cytoplasmic tail of the severe acute respiratory syndrome coronavirus spike protein contains a novel endoplasmic reticulum retrieval signal that binds COPI and promotes interaction with membrane protein. J Virol *81*, 2418-2428.

McCullough, J., Frost, A., and Sundquist, W.I. (2018). Structures, Functions, and Dynamics of ESCRT-III/Vps4 Membrane Remodeling and Fission Complexes. Annu Rev Cell Dev Biol *34*, 85-109.

Miettinen, H.M., Matter, K., Hunziker, W., Rose, J.K., and Mellman, I. (1992). Fc receptor endocytosis is controlled by a cytoplasmic domain determinant that actively prevents coated pit localization. J Cell Biol *116*, 875-888.

Miettinen, H.M., Rose, J.K., and Mellman, I. (1989). Fc receptor isoforms exhibit distinct abilities for coated pit localization as a result of cytoplasmic domain heterogeneity. Cell *58*, 317-327.

Mouquet, H., Scharf, L., Euler, Z., Liu, Y., Eden, C., Scheid, J.F., Halper-Stromberg, A., Gnanapragasam, P.N., Spencer, D.I., Seaman, M.S.*, et al.* (2012). Complex-type N-glycan recognition by potent broadly neutralizing HIV antibodies. Proc Natl Acad Sci U S A *109*, E3268-3277.

Pallesen, J., Wang, N., Corbett, K.S., Wrapp, D., Kirchdoerfer, R.N., Turner, H.L., Cottrell, C.A., Becker, M.M., Wang, L., Shi, W.*, et al.* (2017). Immunogenicity and structures of a rationally designed prefusion MERS-CoV spike antigen. Proc Natl Acad Sci U S A *114*, E7348-E7357.

Pardi, N., Tuyishime, S., Muramatsu, H., Kariko, K., Mui, B.L., Tam, Y.K., Madden, T.D., Hope, M.J., and Weissman, D. (2015). Expression kinetics of nucleoside-modified mRNA delivered in lipid nanoparticles to mice by various routes. J Control Release *217*, 345-351.

Polack, F.P., Thomas, S.J., Kitchin, N., Absalon, J., Gurtman, A., Lockhart, S., Perez, J.L., Perez Marc, G., Moreira, E.D., Zerbini, C.*, et al.* (2020). Safety and Efficacy of the BNT162b2 mRNA Covid-19 Vaccine. N Engl J Med *383*, 2603-2615.

Pornillos, O., Alam, S.L., Rich, R.L., Myszka, D.G., Davis, D.R., and Sundquist, W.I. (2002). Structure and functional interactions of the Tsg101 UEV domain. EMBO J *21*, 2397-2406.

Powell, A.E., Zhang, K., Sanyal, M., Tang, S., Weidenbacher, P.A., Li, S., Pham, T.D., Pak, J.E., Chiu, W., and Kim, P.S. (2021). A Single Immunization with Spike-Functionalized Ferritin Vaccines Elicits Neutralizing Antibody Responses against SARS-CoV-2 in Mice. ACS Cent Sci *7*, 183-199.

Ranieri, E., Popescu, I., and Gigante, M. (2014). CTL ELISPOT assay. Methods Mol Biol *1186*, 75-86.

Reed, L.J., and Muench, H. (1938). A Simple Method of Estimating Fifty Per Cent Endpoints12. American Journal of Epidemiology *27*, 493-497.

Robbiani, D.F., Gaebler, C., Muecksch, F., Lorenzi, J.C.C., Wang, Z., Cho, A., Agudelo, M., Barnes, C.O., Gazumyan, A., Finkin, S.*, et al.* (2020). Convergent antibody responses to SARS-CoV-2 in convalescent individuals. Nature *584*, 437-442.

Rock, K.L., Reits, E., and Neefjes, J. (2016). Present Yourself! By MHC Class I and MHC Class II Molecules. Trends Immunol *37*, 724-737.

Sun, W., He, L., Zhang, H., Tian, X., Bai, Z., Sun, L., Yang, L., Jia, X., Bi, Y., Luo, T.*, et al.* (2021). The self-assembled nanoparticle-based trimeric RBD mRNA vaccine elicits robust and durable protective immunity against SARS-CoV-2 in mice. Signal Transduct Target Ther *6*, 340.

Syed, A.M., Taha, T.Y., Tabata, T., Chen, I.P., Ciling, A., Khalid, M.M., Sreekumar, B., Chen, P.Y., Hayashi, J.M., Soczek, K.M.*, et al.* (2021). Rapid assessment of SARS-CoV-2-evolved variants using virus-like particles. Science *374*, 1626-1632.

van der Horst, A., Simmons, J., and Khanna, K.K. (2009). Cep55 stabilization is required for normal execution of cytokinesis. Cell Cycle *8*, 3742-3749.

van Gils, M.J., Lavell, A., van der Straten, K., Appelman, B., Bontjer, I., Poniman, M., Burger, J.A., Oomen, M., Bouhuijs, J.H., van Vught, L.A.*, et al.* (2022). Antibody responses against SARS-CoV-2 variants induced by four different SARS-CoV-2 vaccines in health care workers in the Netherlands: A prospective cohort study. PLoS Med *19*, e1003991.

Votteler, J., and Sundquist, W.I. (2013). Virus budding and the ESCRT pathway. Cell Host Microbe *14*, 232-241.

Walls, A.C., Park, Y.J., Tortorici, M.A., Wall, A., McGuire, A.T., and Veesler, D. (2020). Structure, Function, and Antigenicity of the SARS-CoV-2 Spike Glycoprotein. Cell *181*, 281-292 e286.

Wang, Z., Muecksch, F., Cho, A., Gaebler, C., Hoffmann, H.H., Ramos, V., Zong, S., Cipolla, M., Johnson, B., Schmidt, F.*, et al.* (2022). Analysis of memory B cells identifies conserved neutralizing epitopes on the N-terminal domain of variant SARS-Cov-2 spike proteins. Immunity *55*, 998-1012 e1018.

West, A.P., Jr., Scharf, L., Horwitz, J., Klein, F., Nussenzweig, M.C., and Bjorkman, P.J. (2013). Computational analysis of anti-HIV-1 antibody neutralization panel data to identify potential functional epitope residues. Proc Natl Acad Sci U S A *110*, 10598-10603.

Wu, K., Werner, A.P., Koch, M., Choi, A., Narayanan, E., Stewart-Jones, G.B.E., Colpitts, T., Bennett, H., Boyoglu-Barnum, S., Shi, W.*, et al.* (2021). Serum Neutralizing Activity Elicited by mRNA-1273 Vaccine. N Engl J Med 10.1056/NEJMc2102179.

Zakeri, B., Fierer, J.O., Celik, E., Chittock, E.C., Schwarz-Linek, U., Moy, V.T., and Howarth, M. (2012). Peptide tag forming a rapid covalent bond to a protein, through engineering a bacterial adhesin. Proc Natl Acad Sci U S A *109*, E690-697.

Zhang, Z., Mateus, J., Coelho, C.H., Dan, J.M., Moderbacher, C.R., Galvez, R.I., Cortes, F.H., Grifoni, A., Tarke, A., Chang, J.*, et al.* (2022). Humoral and cellular immune memory to four COVID-19 vaccines. Cell *185*, 2434-2451 e2417.

Zheng, C., Shao, W., Chen, X., Zhang, B., Wang, G., and Zhang, W. (2022). Real-world effectiveness of COVID-19 vaccines: a literature review and meta-analysis. Int J Infect Dis *114*, 252-260.